Mode-Matched Fiber Fabry-Pérot Cavities for Quantum Technologies

Madhavakkannan Saravanan

Masterarbeit in Physik
angefertigt im Institut für Angewandte Physik

vorgelegt der
Mathematisch-Naturwissenschaftlichen Fakultät
der
Rheinischen Friedrich-Wilhelms-Universität
Bonn

November 2020

I hereby declare that this thesis was formulated by myself and that no sources or tools other than those cited were used.

Bonn, 24 Nov 2020
....
Date

....
Signature

1. Gutachter: Prof. Dr. Dieter Meschede
2. Gutachter: Prof. Dr. Sebastian Hofferberth

Acknowledgements

First of all, I would like to thank Prof. Dieter Meschede for giving me the opportunity to join his research group. I am thankful for the opportunity to extend theoretical knowledge with hands-on lab experience throughout my master studies. The lab work and daily discussions during the master thesis, furthermore, provided great insight into the fascinating field of quantum optics. In addition, I thank Prof. Sebastian Hofferberth for being my second advisor.

I am grateful to Dr. Wolfgang Alt for countless enlightening discussions. The detailed explanations clarified many technical steps in a comprehensive and also understandable way.

A big thanks goes to Dr. Deepak Pandey and Dr. Hannes Pfeifer and Carlos Saavedra for teaching me the lab basics and for the numerous discussions of measurements.

Furthermore, I want to thank Pooja Malik, Santhosh Surendra, Maximilian Ammenwerth, Lukas Ahlheit and Eduardo Urunuela for the discussions (physics and otherwise) that made coming to the office hardly a routine.

Special thanks to my friends, Anuvind Asokan, Naga Teja, Hashika Arjun my companions who have been a great support throughout my thesis.

Finally, I want to thank my family for their unconditional love and support.

Contents

Introduction

In 1917, Albert Einstein proposed that there are three processes, spontaneous emission, stimulated emission and absorption occurring in the formation of an atomic spectral line [1] . Later, in 1946, Purcell et al measured a huge decay time reduction of a nuclear spin excitation after coupling a spin excitation in the paraffin to a microwave cavity [2]proving that, the spontaneous emissions is influenced by the surrounding. It gave birth to the field of Cavity Quantum Electro Dynamics (CQED). By coupling to cavities, it is possible to increase the light-matter interaction to the single photon and single quantum emitter [3]. One of the most important figures of merit to characterize the enhanced light-atom interaction in a cavity is the cooperativity $C = g^2/2\kappa\gamma$, where g is the coupling strength between atom and cavity, κ is the decay rate of the intracavity field and γ is the exited state decay rate [4]. The coupling strength is related to the mode volume of the cavity by $g \propto V^{-1/2}$, where V the mode volume. Small mode volumes give high coupling strengths and having a small cavity reduces the mode volume and increases the coupling strength. One of the smallest Fabry Pérot Cavities is a Fiber Fabry Pérot Cavities (FFPC)

FFPCs are miniaturized optical resonators that are fabricated using laser-ablated spherical end facets with dielectric mirror coatings. These cavities have mode waists on the order of 5 μm. This small mode waists result in a small mode volume which makes them a predestined platform to interface with quantum emitters. Other advantages of FFPCs are small size and an inherent fiber coupling to the cavity. Their compact size and integrability make them promising candidates for integration in quantum networks [5]. They have been implemented as photonic interfaces with various kinds of quantum systems including cold atoms [6], ions [3], solid-state emitters [7] and optomechanical systems [8].

Despite several advantages, FFPCs suffer from a mode miss match between the light mode from the fiber and the cavity mode. This reduces the efficiency at which photons can be coupled to and extracted from quantum emitter inside the cavity. The mode mismatch has two components, one stemming from the different size of the mode field diameter in the fiber and the size of the cavity mode on the mirror. The second is a mismatch in the wavefront curvature, being flat on the side of the fiber mode and at the size of the mirror's radius of curvature on the cavity side. This deficiency in coupling can be overcome by shaping the beam that is incident from the fiber side onto the mirror, using the fiber stacks that include graded index fiber as presented by G.K. Gulati et al in [9]. Using this concept it will also be possible to build longer fiber cavities that are advantageous in ion trapping , where the influence of surface charges of the fibers are needed to be minimised. They can also be used for

spectral filtering and cavity enhanced spectroscopy [10]. This requires precise cleaving and splicing of different fibers, characterization of the propagation through these assemblies and laser machining techniques to produce spherical end facets. In our group the techniques to cleave and splice fibers of different type have been developed by David Röser [11], and the laser machining setup was built by Michael Kubista in his masters thesis [12].

In my master thesis I improved the characterization and manufacturing of fiber assemblies, modelled the light propagation inside assemblies, fabricated mirror substrate surfaces on the end-facets of the assemblies and finally built an FFPC with improved mode matching. In the following chapters, I discuss the theoretical fundamentals of an FFPC and the idea of mode matching. The techniques used to make these fiber assemblies will be discussed and the characterization setup that was built to characterize the beam profiles of the out coupled light will be described. Systematic characterization of the imperfections that can occur during the fabrication process will be provided and finally the results for building a mode-matched FFPC will be presented.

Fiber Fabry-Pérot Cavities

2.1 Optical Fabry-Pérot Resonators

An optical resonator is a setup of two high reflecting mirrors arranged facing each other centred along their optical axis. The light coupled into the cavity through one of the mirrors bounces back and forth between the mirrors. This forms standing wave optical cavity resonator. The intracavity resonance frequencies are separated by $c/2L_{cav}$ where, L_{cav} is the length of the cavity, and c is the speed of light [13]. This intrinsically acts as a wavelength selector where the electric fields of different wavelengths interfere destructively to allow resonance wavelengths that satisfies the boundary condition $L = q\lambda/(2n)$. Here, q is the number of intensity maxima in the cavity and λ is the wavelength of the light and n is the refractive index of the medium inside the cavity [14]. Throughout our experiment, the medium inside the cavity is air and hence the refractive index $n = 1$. This spacing between the two successive intensity maxima is defined as the Free Spectral Range (FSR) (Fig: 2.1 b)) of the Optical cavity $\Delta\lambda_{FSR} = \lambda^2/L$ [14]. This results in a comb like spectrum inside the fiber resonator. The intracavity power of a resonator can be expressed as,

$$P_{circ} = P_{in}T_1 \frac{\mathcal{F}^2}{\pi^2} \frac{1}{1 + 4\frac{\mathcal{F}^2}{\pi^2}\sin^2\left(2\pi\frac{\nu}{2\delta\nu_{FSR}}\right)} \tag{2.1}$$

Here, assuming the reflectivity of the mirrors $R_i = 1 - T_i - L_i$ and $i = 1, 2$; T_i is the transmission of the mirror and we have assumed the losses in the mirror $L << 1$. The factor $\mathcal{F} = 2\pi/(T_1 + T_2 + 2L)$ is the finesse of the cavity; a measure of the optical quality of the mirrors [15]. A simplified overview of the electric fields involved in a cavity setup is depicted in Fig 2.1 a) and the intracavity spectrum is shown in Fig 2.1 b) for two different $\mathcal{F}$.

2.1.1 Cavity Stability

A cavity formed with two flat mirrors is prone to small miss alignments of the mirrors and hence, the cavity becomes very sensitive to microscopic vibrations and cannot be kept stable for long times. A solution for this would be to use concave mirrors with certain Radius Of Curvatures (ROC) with which the light ray entering the resonator can be confined and are less sensitive to small angular deviations and microscopic vibrations on the mirrors. The stability also depends on the length L_{cav} of the optical
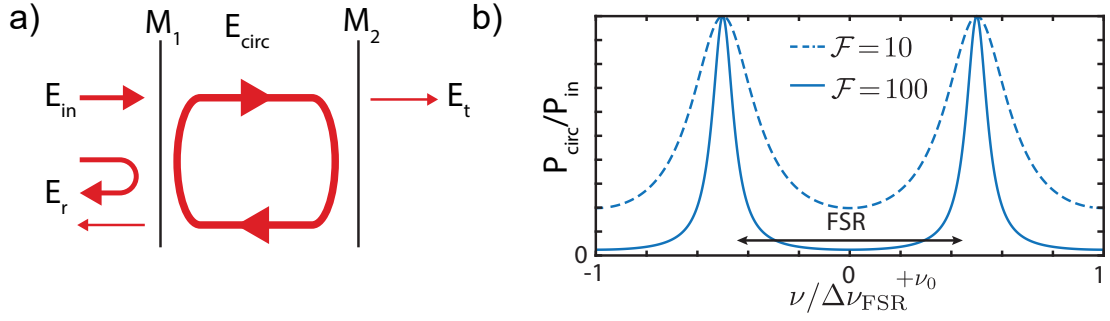
Figure 2.1: a) shows the simplified overview of the electric fields present in a cavity. b) shows the intracavity power spectrum with resonance peaks separated by a free spectral range for a low finesse and a high finesse cavity.

cavity [13]. These figures were taken from [15]

For such resonators, the stability condition is given by,

$$0 \leq g_1 g_2 \leq 1 \tag{2.2}$$

where, g_i is the g-factor of the mirrors, $g_i = 1 - \frac{L}{ROC_i}$ [13].

In Fig: 2.1 b), various cavity setups are depicted together with their corresponding g-factors. In our experiment we build two types of cavities. A confocal cavity, where two concave mirrors form a cavity and a hemispherical cavity, where a plane mirror is used together with a concave mirror.

2.1.2 Cavity Modes

The electric field distribution of the light field formed insidethe cavity depends on the geometry of the cavity mirrors. When spherical mirrors are used to build the cavities, the steady-state electric field intensity profile are the solutions of paraxial Helmholz equation with boundary conditions that the wavefronts match the geometry of the mirrors. The fundamental TEM_{00} mode in a cavity is shown in Fig 2.2 The spatial intensity profile of this fundamental Gaussian beam is given by,

$$I(x, y, z) = I_0 \frac{w_0}{w_z} \exp\left(-2 \frac{x^2 + y^2}{w(z)^2}\right) \sin^2(kz). \tag{2.3}$$

Here, w_0 is the minimum waist of the beam and z_R is the Rayleigh range given by $z_R = \pi w_0^2 / \lambda$. The waist of the beam diverges as it propagates, which is given by $w(z) = w_0^2(1 + z^2/z_R^2)$. During all the measurements, we use $\lambda = 780$ nm infrared laser. For a cavity as shown in Fig 2.2 the waist w_0 is fixed by the geometry of the mirrors, the waist, w_0 can be expressed in terms of the cavity g factors as [17],

$$w_0^2 = \frac{L_{cav}\lambda}{\pi} \sqrt{\frac{g_2 g_2 (1 - g_1 g_2)}{(g_1 + g_2 - 2g_1 g_2)^2}} \tag{2.4}$$
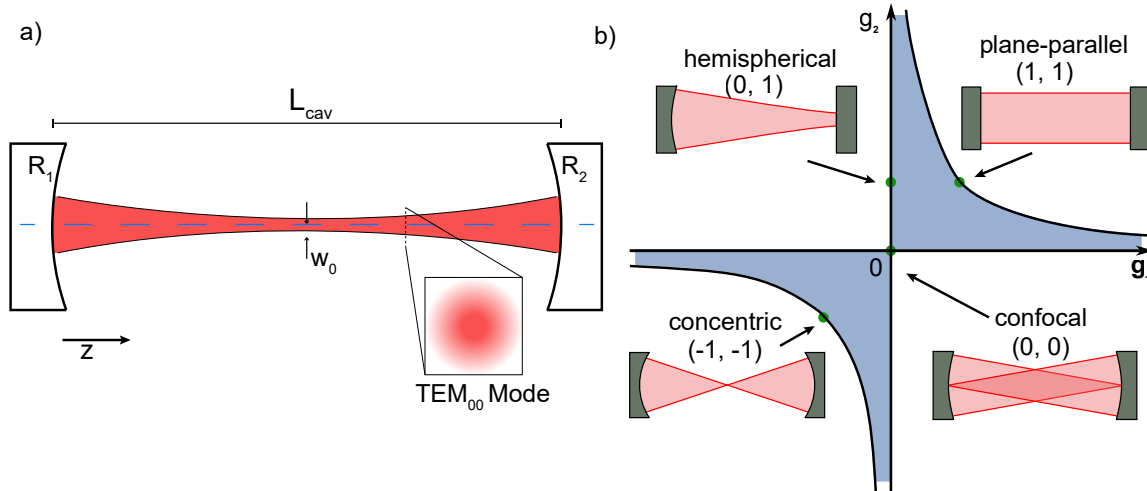
4

Figure 2.2: a) A confocal cavity with the fundamental *TEM*$_{00}$ mode is shown. The light field inside the cavity is a fundamental Gaussian mode. In b), four cavity setups are depicted and their respective g-factors, one for each mirror, are given. The shaded region indicated the stable region based on the cavity geometry. This figure is modified from [16]

2.2 Optical Fibers

Optical fibers are dielectric waveguides that guide the light beam over long distances. They are usually made out of fused silica doped with different materials (e.g. germanium dioxide) to have different refractive indices. These fibers have a cylindrical core with a higher refractive index covered by a low refractive index cladding. When the light beam coupled into the core gets totally internally reflected and is guided through these fibers. Optical fibers are used for transmitting light over long distances as they are thin, flexible and have reasonably small losses. The outcoupled light from these optical fibers are to a very good approximation Gaussian beams. In our experiment we use a constant fiber diameter of 125 μm for all the fibers.

2.2.1 Types of Fibers

Based on the refractive index profiles of the core, the fibers can be classified into different types.

Step index fibers: Step index fibers have uniform refractive index at their core and a uniform refractive index at the cladding with a sharp transition from the core to the cladding. Due to this the light beams are total internally reflected and are guided through the fibers. These fibers can also be used as spacial mode filters. Based on core diameters there are two types.

Single Mode (SM)   fibers are fibers that have a small core diameter less than 10 μm. They are optimum for guiding a single light mode efficiently over very long distances. Due to their small core diameter, the incoupling efficiency of free space laser beams is limited. In our experiments we use the
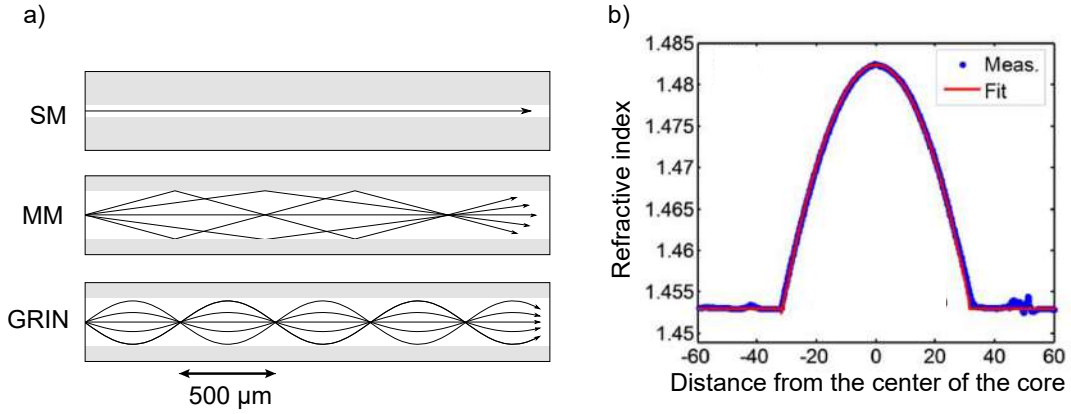
a)

b)

Figure 2.3: a) shows the ray propagation of light within different fibers. This image is taken from Ref [12]. b) shows the refractive index profile of the core of the ThorLabs GIF 625 GRIN fiber. This image is taken from Ref [18]

SM fiber 780HP from ThorLabs with a core diameter of 4.5 μm and the refractive index of the core is $n_{SM} = 1.46$ and a mode field diameter $(1/e^2)$ of the out coupled beam of (5.0 ± 0.5) μm.

Multi Mode (MM) fibers have a larger core diameterbetween 50 μm to 70 μm. Due to this large diameters, as their name suggests, they guide multiple modes of light and therefore, are suitable to guidelight from less coherent sources.

Graded Index (GRIN) fibers The GRIN fibers, in first order approximation, have a quadratic refractive index profile in the core given by,

$$n(r < a) = n_1 \left[1 - \Delta \left(\frac{r}{a} \right)^2 \right] \quad (2.5)$$

$$n(r > a) = n_2$$

Here, r is the radis, a is the core diameter and $\Delta = \frac{(n_1 - n_2)}{n_1}$. The refractive index decreases quadratically from the center of the core to the edge.
They have similar properties like the MM fibers with larger core diameters. In our experiments we use two types of GRIN fibers, i) ThorLabs GIF 625 and ii) Corning GRIN fibers. In our experiment all the characterizations and modelling were done using the ThorLabs GIF 625 GRIN fiber that has a core diameter of 62.5 μm. The refractive index profile of this fiber was characterized in [18] and is shown in Fig 2.3. Due to this refractive index profile, the light beam inside the core converges and diverges periodically while propagating inside the fiber. In this thesis, the length that the beam propagates between two convergences is called as the refocusing length of the GRIN fiber and for Thorlabs GIF 625 the refocusing length was 500 μm.
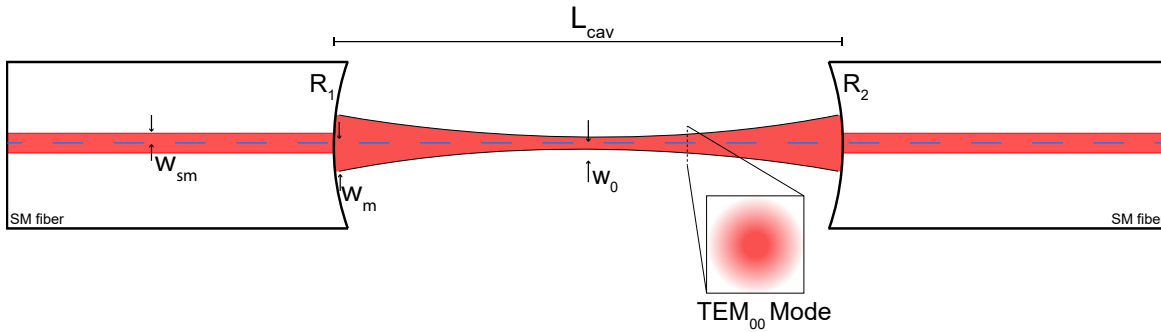
6

Figure 2.4: This figure shows the overview of a FFPC built with two SM fibers. The waist at the mirror w_m is larger than the waist of the SM fiber resulting in a poor coupling of the cavity cavity mode into the fiber.

2.3 Fiber Fabry-Pérot Cavities

Fiber Fabry-Pérot cavities (FFPCs) are optical resonator that are built using mirrors made on the fiber end facets. The end facet of the fiber is ablated to imprint spherical structures and high reflective mirror coatings are applied. Using two such fiber mirrors a FFPC can be assembled. The schematics of such an FFPC is shown in Fig 2.4. They have several advantages over macroscopic cavities. FFPCs have miniature size, so it can be fit into vary small spaces, inherent fiber coupling and very small mode volumes, enabling high electric fields to interface quantum emitters. Similar to macroscopic cavities, in FFPCs the fundamental mode is the TEM_{00} Gaussian mode. One of the major disadvantages of such a FFPC is the mode miss match of the cavity mode and the mode of the light coupled out of the fiber. FFPCs are usually built using SM fibers and because of the small mode field diameters of the SM fibers, the light beam that is coupled out of the SM fiber has a small waist w_{SM} in the order of 5 µm. The waist of the light mode at the cavity mirror w_m is larger than the waist of the outcoupled SM fiber is shown in Fig 2.4. Hence the light from the cavity cannot be coupled back into the SM fiber efficiently. At the same time the wave fronts of the cavity mode and the light modes also do not match. This mode miss match leads to losses light outcoupled from the cavityand it also limits the cavity length L_{cav} that can be built as the light coupled out of the SM fiber diverges strongly.

2.3.1 Clippling losses in FFPCs

The finesse of a resonator is a measure of the optical quality of its mirrors and, as described in Sec 2.1, is inversely proportional to the power losses upon reflection. The transmission T and the losses L are specific to the coatings and are not specific to the geometry of the mirrors. In case of FFPCs as the the spherical structures are ablated with laser beams, their Gausssian-like structure causes losses per mirror defined by C [19].

$$C = exp\left(-\frac{2(R)^2}{4w_m^2}\right) \tag{2.6}$$

Here, Ris the ROC of the ablated spherical structure. Due to the limits of ROCs that can be ablated, when the length if the cavity is increased the diverging beam gets clipped at the end facets. This results in a drop of the finesse due to clipping losses. The finesse of an FFPC is defined for a mirror of
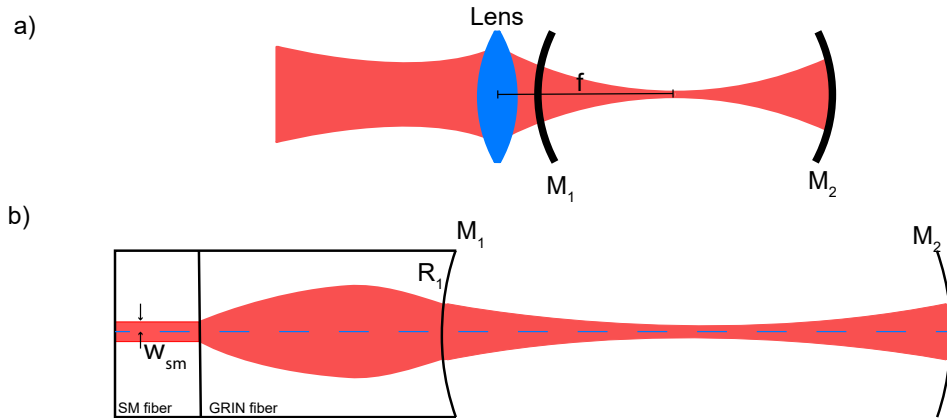
Figure 2.5: a) shows how the mode matching is achieved in free space using a lens. b) shows the stack of SM GRIN fiber assembly, and the GRIN fiber acts as the lens to achieve mode matching in FFPCs.

ROC R as,,

$$\mathcal{F} = \frac{2\pi}{T + L + C(L_{cav}, D, R)} \tag{2.7}$$

2.3.2 Mode Matching in FFPCs

For an optical cavity in free space, a high input coupling of light is obainted by shaping the input beam using a lens so that it matches with the mode of the cavity. By placing the lens at the right distance away from the cavity mirrors mode matching of the cavity mode and the light mode can be achieved along with the wavefront matching, as shown in Fig 2.5 a). A similar solution has to be formulated for FFPCs while keeping the advantages of the FFPCs.

 The mode matching in FFPCs is achieved using the GRIN fibers [19], by utilizing their characteristic of periodic convergence and divergence of light along the fiber Fig 2.3, we can cleave the fiber at the appropriate length to set the mode waist at the enf facet. The refocusing length of the ThorLabs GIF 625 500 μm; if the GRIN length of 250 μm (half refocusing length) is spliced to a SM fiber, the beam entering the GRIN from the SM fiber expands to have a larger beam waist. If a GRIN length of more than 250 μm is used, the beam starts to focus and has a lesser waist at the end facet. This way by selecting the right GRIN length the waists of the light mode entering the cavity can be controlled. The waists of the light mode and the waist of the cavity mode can be matched at the mirror. On such a fiber assembly, by ablating the end facet of the GRIN fiber with ROC in accordance to the wavefront curvatures of the intracavity light field, we can achieve good wavefront matching. Thus the beam waists and wavefronts can be matched in the cavity while maintaining the advantages of the FFPC.

Fiber Assembly and Characterization

In this chapter the fabrication of a SM GRIN fiber assembly and ablation procedure to produce end facets with spherical depression are presented. A microscope beam profiling setup for the characterization of the beam profiles emitted from these assemblies was setup. The characterisation automation of this setup will be discussed along with an example of a complete beam profiling cycle.

3.1 Fiber assembly

A fiber assembly in our experiment is a stack of different types of fibers. For the major part of this thesis a GRIN fiber piece is connected a SM fiber Fig 3.1 to form a stack. To produce such assemblies fibers have to be spliced and cleaved to have a specific GRIN length with an accuracy of $< 2\,\mu m$ and the cleave angle (angle between the surface normal of the end facet and the fiber axis) is below a threshold $(< 0.8°)$ as shown in the Fig 3.1 and the cleave lengths have to be accurate to $< 2\,\mu m$. Flat end facets are also important during the laser ablation process to produce good spherical surface on the end facets, ripples and tilted facets can reduce the quality of the final mirror surfaces, leading to decentrations and reduce the coupling to the fiber guided mode. The influence of various fabrication imperfections will be discused in detail in Sec 4.2. The detailed procedure of cleaving and splicing will be discussed in this section.

3.1.1 Cleaving

The cleaves are done using a Fukikura cleaver CT-101. The cleaver was modified to produce precise cleave lengths by David Röser in his master thesis [11]. The schematic sketch of the cleaver is as shown in Fig 3.2 a). The fiber that has to be cleaved is stripped off of the coating and is cleaned and clamped on the fiber holder. To produce a cleave, a stripped and cleaned fiber is held on the bench and the fiber tightening clamp. Then, the tensioned fiber is hit by the blade, which breaks it into two pieces with ideally flat, straight end facets. An interferometric reconstruction of the fiber end facet is as shown in the Fig 3.9 a).
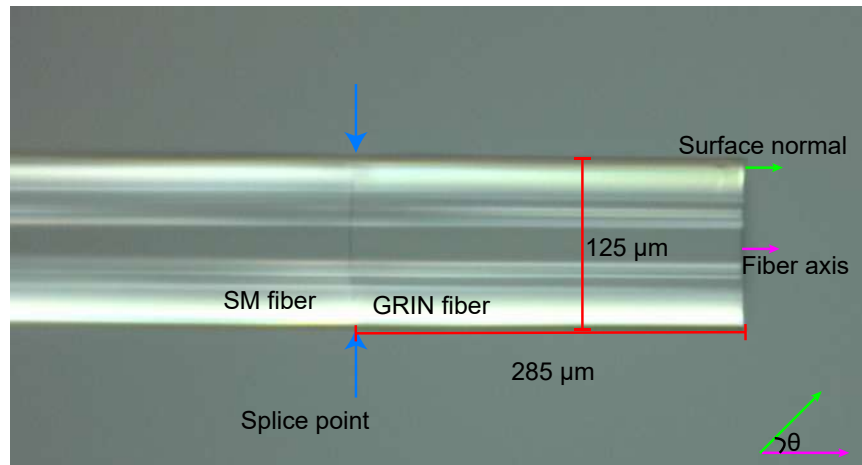
Figure 3.1: This figure shows the microscope image of a SM grin assembly after the cleaving and splicing procedure. The cleave length of the GRIN fiber used here is set to 285 µm which was measured with respect to the fiber diameter 125 µm The angle between the axis of the assembly and the surface normal of the fiber end facet is the cleave angle of the fiber shown as θ in this figure.

3.1.2 Splicing

To produce assemblies with different fiber types, the cleaved end facets of two fibers need to be spliced together. This is done using Fijikura ARC Master FSM-100P+, a fully automated fusion arc splicer. The schematic sketch of the splicer is shown in Fig 3.2 b). The cleaved fibers are placed on the motorized platforms with the same fiber holders as used in the previous cleaving step. After an automatic alignment of the fiber ends, an electric arc is produced between the two end facets. The motorized arms bring the fibers into contact and pushes them into each other by a given distance the Splice Overlap Region (SOR). We found that the SOR needs to be at least 10 µm large to produce stable splice points. An optimization of the various process parameters of the splicing was done by David Röser in his master thesis [11].

3.1.3 Producing SM-GRIN assembly

As discussed in Sec 2.3.2 the refocusing length of the out coupled light can be controlled by setting the GRIN length. SM-GRIN assemblies of different GRIN lengths are produced with the following procedure.

Step 1:   The SM and the GRIN fibers are cleaned and cleaved . Without removing them from their respective holders the fibers are taken to the splicer. The initial position of the cleave bench is recorderd using an USB microscope that tracks a mark on the moving arm.

Step 2:   The cleaved fibers are spliced with a splice overlap region of 10 µm. Once the splice is done the the GRIN fiber's holder is opened. The spliced SM and GRIN fiber are still clamped on the SM fiber's holder. This is taken back to the cleaver.
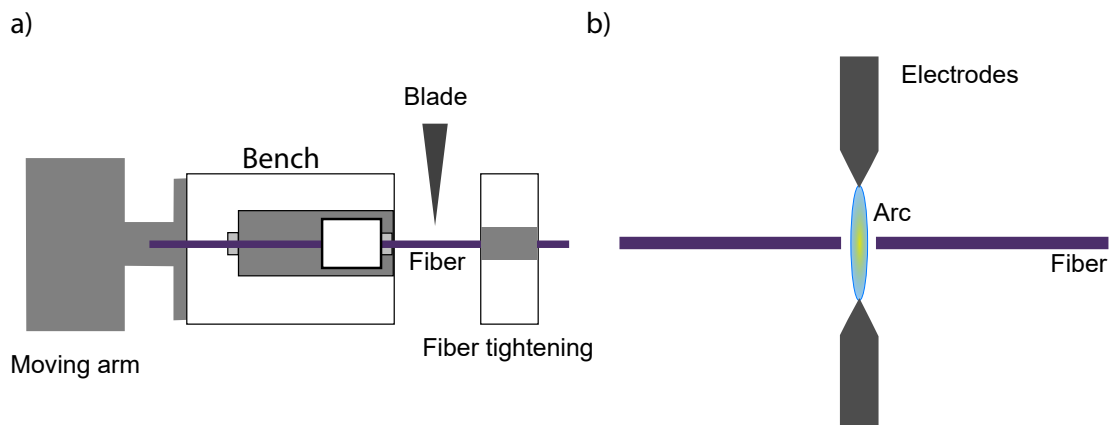
Figure 3.2: a) the fiber is placed with its fiber holder on the bench and clamped on the opposite side. The blade hits the tensioned fiber to produce the cleave. The cleave length can be changed by adjusting the position of the bench using the moving arm that is controlled via a micrometer screw. b) Shows the sckematic sketch the splicer, the electrodes are used to produce an electric arc that melts the fibers and that are then pushed together to produce the splice.

Step 3: The bench of the cleaver is moved away by a defined length from the blade to the final position by the micrometer controlled arm. The difference between the initial and the final position of the bench gives the GRIN length of the assembly. The holder with spliced SM and GRIN fiber is placed back on the bench and cleave is performed to produce a SM-GRIN assembly of desired GRIN length as shown in Fig 3.1.

Once these fiber assemblies are prepared, they have to be tested to determine the shape of the out-coupled beam. This was initially done using a knife edge measurement setup as shown in Fig 3.3. There, the beam shape is reconstructed by scanning a blade across the beam (Y direction in Fig 3.3) and recording the optical power (using PD_t in Fig 3.3) that is still transmitted at different positions after the fiber end facet (Z direction) . The local beam radius along Y is reconstructed by fitting error functions to the transmitted power for each y axis scan. An exemplary measurement is shown in Fig 3.3 b). Using a knife-edge measurement to characterize the assemblies has however several disadvantages. A full characterization with the knife-edge setup takes about 7-10 hours, which makes it unsuitable for testing larger sets of fiber assemblies. Also vibrations and drifts for example due to temperature changes over the long measurement time affect the accuracy of the measurements. Moreover, the knife-edge measurement only gives information about a single transversal axis of the beam. Beam ellipticities or aberrations will not be recognized. In order to speed up the characterization of the produced assemblies and to gain more information on the full three dimensional shape of the beam a different measurement technique is therefore required.

3.2 Microscope Beam Profiling System

In order to gain more information on the out-coupled beam shapes and to speed up the measurement process a microscope setup for beam profiling was implemented. The cross section of the beam in
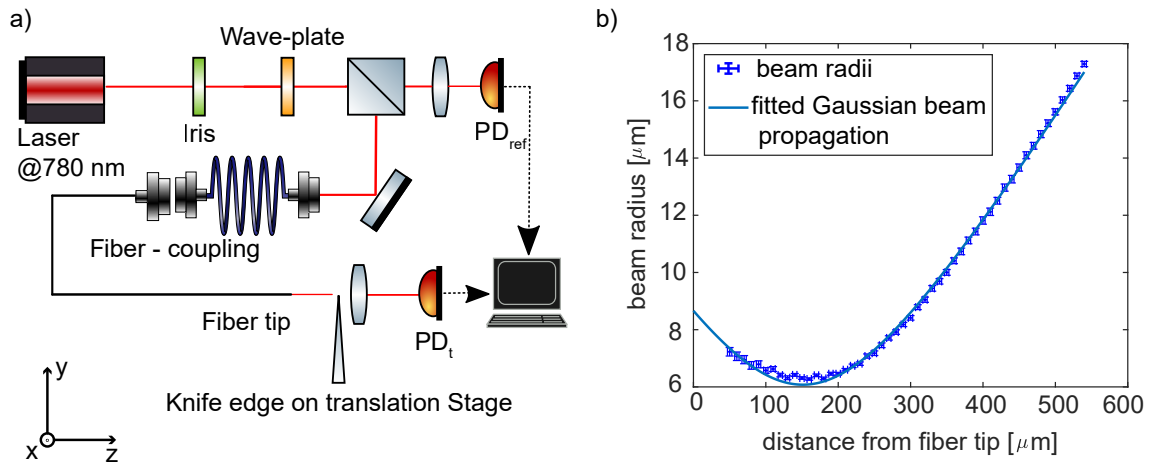
Figure 3.3: a) shows the knife-edge measurement setup that was initially used to characterize the beam propagation . b) shows a reconstruction of the outcoupled beam from a fiber assembly measured using this setup.

the object plane is thereby imaged onto a camera sensor. Scanning the object plane along the beam allows for a full characterization of the emitted beam shapes. As the beam coupled out of the fiber assemblies can focus down to a beam diameter of less than 5 μm the imaging setup needs to magnify the beam cross section that is imaged onto a camera sensor such that the pixel size of the sensor does not limit the characterization.

3.2.1 Beam Profiling Setup

A schematic of the microscope imaging system is shown in Fig 3.4. It consists of Mitutoyo Apochromatic NIR objective "MY20X-824" together with the corresponding 20 cm tube lens images the cross section of the beam in the object plane with a 20x magnification onto the camera sensor. To start a characterization cycle a fiber end facet is moved into the focus of the objective by illuminating it with a flash light and changing the fiber position until a sharp image of the fiber edge and surface can be observed.

3.2.2 Characterization of the Setup

Imaging of light transmitted through a 1 μm sized pinhole was used to benchmark the microscope system, to verify its magnification and to determine if aberrations originating from the imaging setup itself are small enough to use it for the investigation of the beam quality emitted from fiber assemblies. The small size of the pinhole light source leads to a strongly diverging beam that is very sensitive to aberrations of the imaging system and is ideal to evaluate its performance. A collimated beam was focused using a high numerical aperture lens to couple light into the pinhole. This combination of the lens and pinhole was placed on a 3 axis motorised stages in order to move it within the field of view and along the optical axis for characterization.
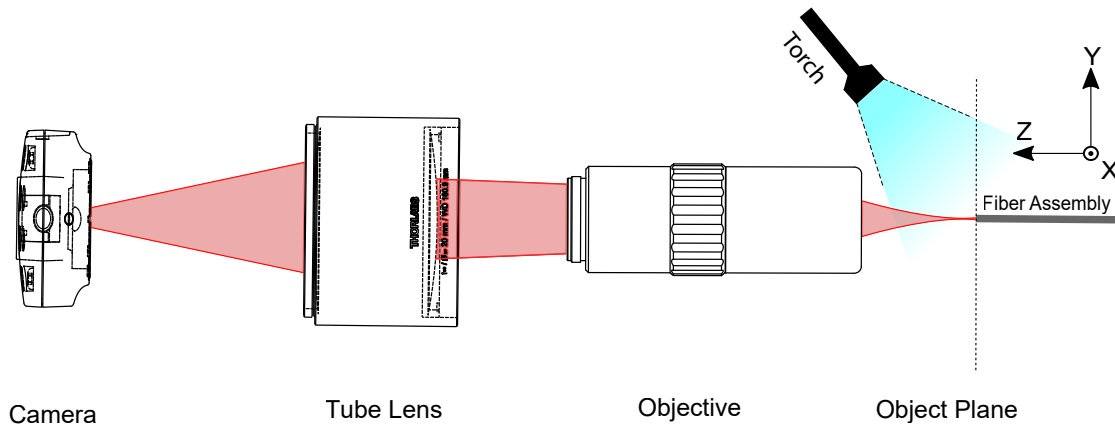
Figure 3.4: This Figure shows the microscope beam profiling setup that was built to characterize the beam propagation of the out coupled light. The torch is used to illuminate the end facet of the assembly in the first step. Next the light is coupled in to the assembly is magnified by the objective and is refocused into the camera sensor using the tube lens

Aberrations were characterized by positioning the pinhole in the focus of the objective and the scanning it transversely within the object plane of the microscope setup and capturing the intensity profiles for the different positions of the beam. The intensity profile of of the image of a pinhole is an Airy function Ai . Hence, the images were subsequently fit using $Ai = (2J_1(\Theta)/\Theta)^2$ where $\Theta = 2\pi r \times NA/\lambda$ where r is the radial coordinate, numerical aperture $NA = 0.5$, and $\lambda = 780nm$ [20] Then the Strehl ratio (S) 3.1 is calculated at each point in the XY-axis of the sensor using.

$$S = \frac{I_{fit}}{I_{max}} \tag{3.1}$$

Here, I_{fit} is the Peak intensity of the fit and I_{max} is the peak intensity in the aquired image.
We observed that the Strehl ratio remained 1±0.2 within the full imaging plane implying negligible abbreation in our setup. A map of the Strehl ratio throughout the object plane is as shown in the Fig 3.5

Another method to qualitatively investigate aberrations is to scan the pinhole along the optical axis. There, aberrations manifest themselves as asymmetric intensity patterns with respect to the focus. Fig 3.6 shows the recorded intensity in a cut along the optical axis that exhibits only very minor asymmetries.

Magnification was characterized by moving the pin hole on the translation stage by known distance. Given the pixel size of 5.2 µm of the Thorlabs DCC1545M camera, the magnification was found as the magnification to be $M = 20.1 \pm 0.4$. Independently it was also confirmed using the measured size of the beam waist emitted from an SM fiber at its end facet and comparing it to the specified mode field diameter of the fiber. After the characterization, the lens-pinhole setup on the translation stages was replaced by a home built holder that that is able to clamp the fiber holder Fujikura FH-100 that is used within the assembly fabrication to incorporate the profiling of the emitted
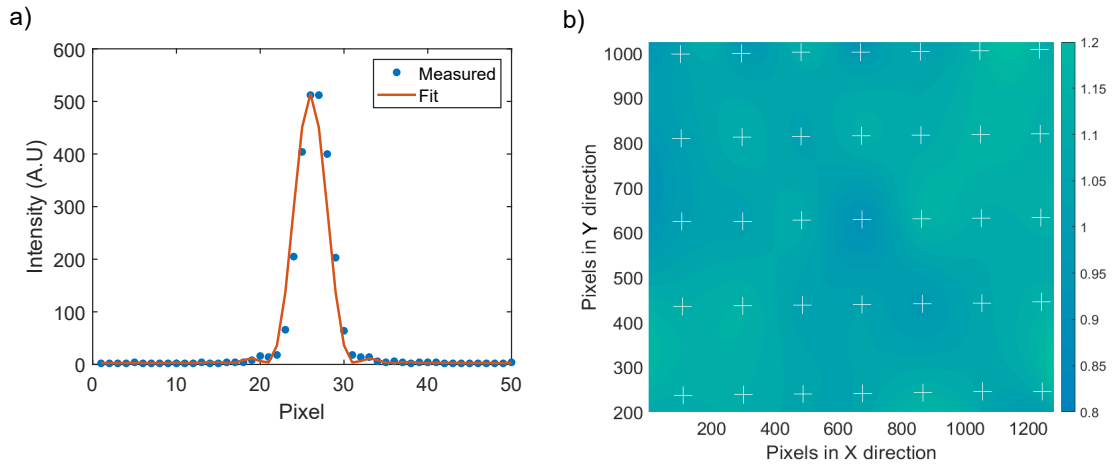
Figure 3.5: a) shows the Airy function pattern of the measured intensity of the pinhole at focus and the fit of the airy function. b) shows the Strehl ratio of the setup throughout the object plane, the crosses are the points where the Strehl ratio was measured and it was extrapolated throughout the sensor

.
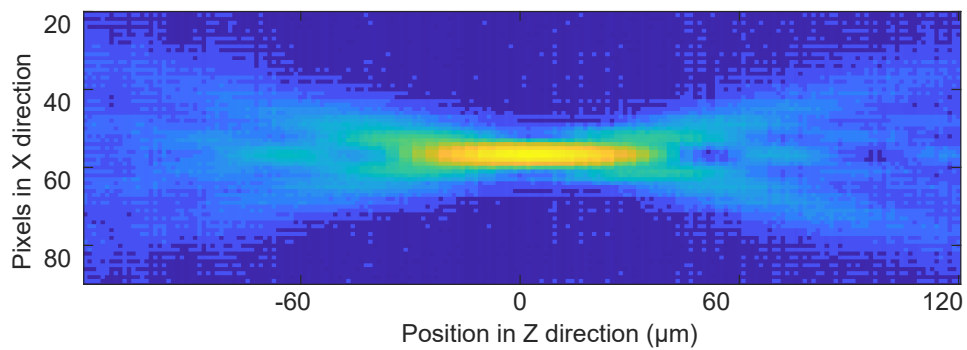
Figure 3.6: This figure shows the lateral intensity of the scan of 1 μm pinhole along Z axis. The pattern shows minimum asymmetries indicating less aberrations.

beams within the fabrication procedure.

3.2.3 Automation and complete characterization cycle

The Newport MFA-PPD, three axis motorised linear translation stages and the ThorLabs infrared camera were both controlled with MATLAB. The characterization is done in three steps,

- Locating the fiber and bringing the end facet to the object plane

- Initialising the characterization and data acquisition using the camera

- Analysis of the acquired data.

Allignment Once an assembly is fabricated, it is placed on the motorized stages. A laser at 780 nm is coupled into the single mode fiber and is emitted from the assembly. Using this out-coupled light the fiber is located and brought in line with the optical axis of the characterization setup. In order to move the end facet into the object plane, the end facet is illuminated using a flashlight and the assembly is scanned in 10 μm steps along the optical axis. The position of the sharpest image of the end facet edge shown in Fig 3.7 pinpoints the object plane of the setup. Now the illumination is turned of and only the light that is emitted from the assembly is used.

Data acquisition Once the end-facet is moved into the object plane the acquisition is started. Subsequently, the fiber is moved out of the object plane while the beam shape as measured on the camera for each position of the fiber is recorded. To compensate the drop of intensity when the beam is imaged away from its focus point, the exposure time of the camera is adjusted. This way the imaging setup can image the beam profile for over a full distance of 2 mm around the beam focus point. The assembly moves away from the object plane in 10 μm steps for 100 steps covering 1 mm and an image is acquired for every position of the fiber along the propagation axis . This data acquisition takes between 300 s and 700 s. Compared to the 6 to 8 hours of a corresponding knife-edge measurement, this is a strong improvement that enables us to test each assembly during different fabrication steps and at the same time gather more information on the full beam shapes. For example, the effect of curved surfaces on the end-facets after laser ablation compared to flat assembly ends was investigated (see Sec 3.4)
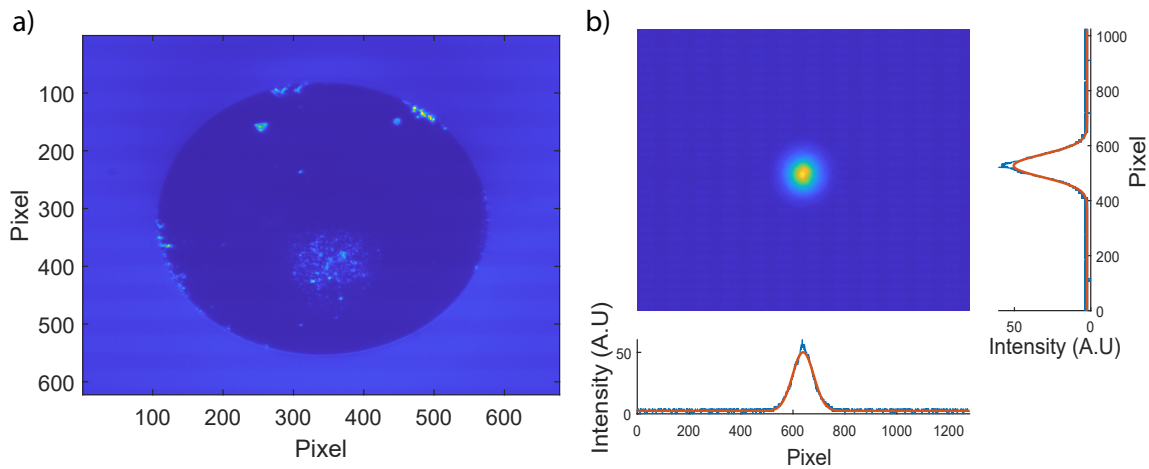

Figure 3.7: a) shows the end facet imaged when located in the object plane and illuminated by a flashlight. b) Shows the Gaussian beam profile of the light emitted from SM fiber at 250 μm away from the object plane. The subplots show the intensities and its fit of the cut through along the maximum value measured by the camera.

Analysis To exclude obvious defective assemblies a rough qualitative assessment of the outcoupled beam shapes is performed. In order to then reduce the full volumetric dataset of recorded intensities, a two dimensional Gaussian intensity pattern is fitted to each image. The $1/e^2$ radius of the intensity pattern versus the assembly position as shown in Fig 3.8 allows to determine the refocusing length of the fabricated assembly.
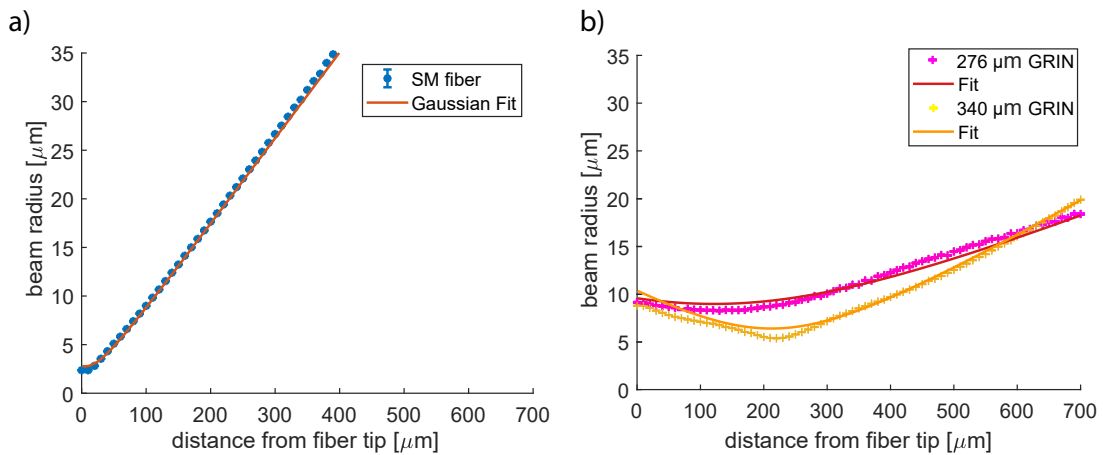
Figure 3.8: a) shows the out coupled beam radius in dependence of the distance from the fiber for a bare SM fiber. b) shows the measured beam radii vs. the distance from the end-facet of the assemblies for two different lengths of the GRIN fiber. The choice of the lenght of the GRIN fiber piece determines the position of the smallest waist and its size.

3.3 Optimization of assembly fabrication parameters

The new beam profile characterization setup allows for the analysis of larger sets of fiber assemblies, which was used to optimize several parameters of the fabrications process. In a first step, the beam quality emitted from assemblies that were fabricated using different GRIN fibers was evaluated. The two most promising candidates were the Thorlabs GIF 625 and the Corning Infinicor GRIN fibers. We observed that the beams emitted from ThorLabs GRIN fiber had more ellipticity compared to the Corning GRIN fiber therefore we chose to use the Corning GRIN fiber for the first two coating runs discussed in Sec 5.1 Within this evaluation also the splicing parameters were optimized yielding e.g. a optimal splice overlap region of 10 um (see Sec 3.1.2).

The cleave tensions were optimized using the interferometer setup built by Michael Kubista [12]. The optimization of the cleave tension led to a tension of 2.1 N m. A reconstructed surface profile of such a cleave is shown in Fig 3.9. Below this value the produced cleaves showed large deflections at the edge. Values above 2.1 N m lead to an increase of the roughness of the produced end-facets.

3.4 Ablating Spherical Surfaces on fiber end facets

Before the assemblies are sent out for a high relfective coating, a depression is ablated on the end-facets as they are later-on used as concave cavity mirrors. The ablation is performed using a CO_2 laser ablation setup ([12],[11]) where high power pulses, whose duration and power are controlled using an AOM, are focused on the fiber end facet. A schematic of the setup is shown in Fig.3.10 The ablation imprints the intensity profile of the laser pulses on the end-facets. The center, near spheric part of the formed depressions defines the later-on concave fiber mirror. By changing the pulse duration, number of pulses and position of the fiber in the focus of the CO_2 laser the size and radius of curvature (ROC) of the produce spheric depression can be adjusted. Together with the Master student, who is working
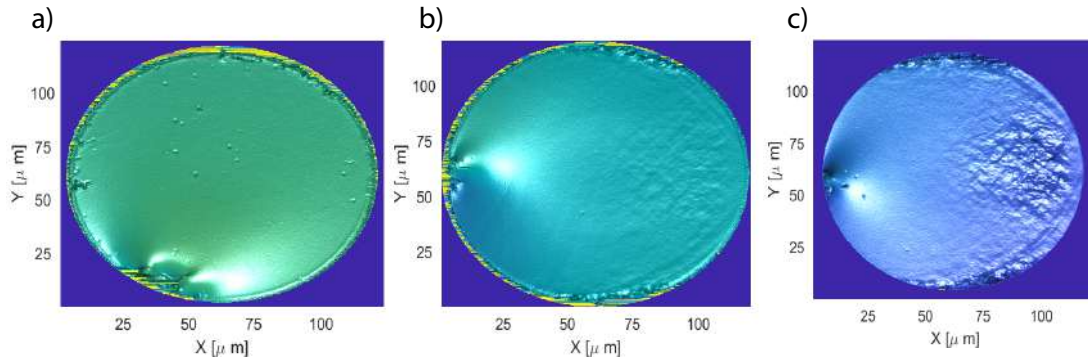
Figure 3.9: The interferometric reconstruction of the end facets to understand surface quality if the fibers cleaved with different cleave tensions is shown in this figure. In all there figures the point at which the blade hits the fiber has deformation. a) shows the end facet of a fiber cleaved with a lesser cleave tension from optimum. We observe huge defects at the spot where the blade hits the fiber. b) shows the optimum cleave tension used, we still see the deformation due to the blade and also the cracked structures on the fiber but both these effects were minimal for this cleave tension. c) shows the endfacet of the fiber cleaved with a high cleave tension we see huge surface roughness at the part opposite to the edge where the blade hits the fiber.
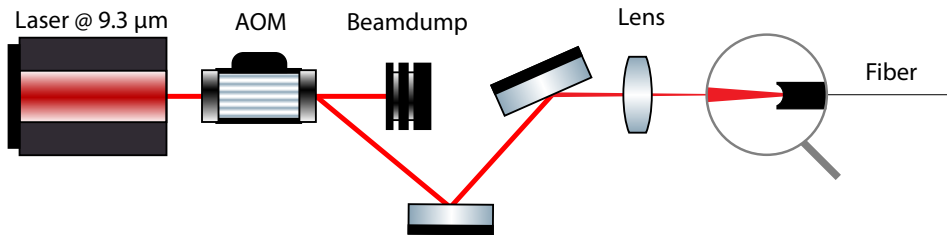

Figure 3.10: This figure shows a schematic of the laser ablation setup used to produce spherical depressions on the end facets. The CO_2 beam is passed through an AOM used to control power and pulsing and is focused to the end facet of the fiber where a spherical depression is ablated.

on the optimization and upgrade of this setup, S. Surendra, we were able to retrieve ROCs ranging from 100 μm - 700 μm. Once the depression is shot on the endfacet, the surface were reconstructed using a white light interferometer setup. An example for the surface profile of an end-facet before and after the application of the laser shots is shown in Fig 3.11

Once the end facets are ablated , the beam propagation through the assemblies was again characterized. The ablation process has a significant effect on the beam propagation out of the assemblies. The changed shape of the end-facet changes the refocusing length of the SM GRIN assemblies. An example for the refocusing behavior from the beam emitted from an SM-GRIN assembly is shown in Fig 3.12.
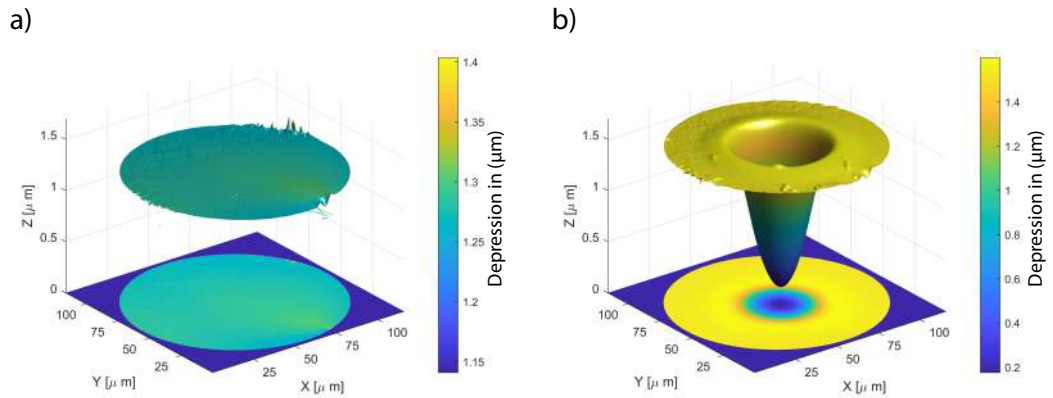
Figure 3.11: This figure shows the interferometric reconstruction of the fiber endfacets before and after shooting, the Z axis in this figure is exaggerated. a) shows the end facet of the cleaved fiber. b) shows the end facet of a shot fiber with the spherical surface that is imprinted on the fiber end facet.
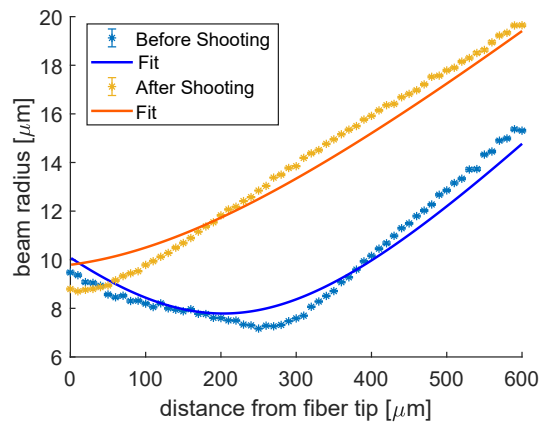
Figure 3.12: This figure shows the beam radius vs distance from a SM-GRIN fiber assembly of the out-coupled light before and after the ablation process. The focus and the position of the refocusing has changed significantly.

In the ideal case, the shot ROC of the spherical part of the depression and the wavefront curvature of the beam emitted from the shot assembly match such that a wavefront mismatch with a future cavity mode is avoided.

Models for mode-matching in FFPC

In this chapter a model to characterize the propagation of the Gaussian beam inside the fiber assembly using the ABCD matrix formalism is described, we use this model to predict the properties of the outcoupled light of the fiber assemblies. This model is also used to calculate the coupling of the back reflected beam from the fiber end facet mirror and the coupling of the overlap of the spatial mode of the output light with the mode of the cavity.

4.1 Ray transfer matrix formalism

With the imaging system described in the Sec 3.2.3 , we were able to efficiently collect information about the outcoupled beam propagation. We started to build a model that can predict the propagation based on the Ray transfer matrix formulation [21]. According to this formulation optical elements like a lens and interfaces can be described by a 2×2 matrices. The gaussian beam can be represented by a complex parameter $q = z + iz_0$, where z_0 is the Rayleigh range and z the distance from the focus position along the optical axis. Thus by knowing the focus position and the radius at focus we can describe a Gaussian beam parameter q at any point in space. The complex parameter q_{out} that comes out of an optical element defined by a ray transfer ABCD matrix with a input parameter q_{in} is given by,

$$q_{out} = \frac{Aq_{in} + B}{Cq_{in} + D} \tag{4.1}$$

Using this equation the output parameter q_{out} of a Gaussian beam propagating through a system of optical elements can be calculated.

4.1.1 The ABCD Matrices

In a fiber assembly the major elements through which the Gaussian beam propagates are interfaces and GRIN fiber. The ABCD matrix of these elements are defined as,

The Interfaces: An optical interface between two optical element is a sharp change in the refractive index along the propagation. When a beam passes through two optical elements with different refractive index the angle of propagation is changed, the corresponding ABCD matrix is

given by

$$\begin{bmatrix} A & B \\ C & D \end{bmatrix} = \begin{bmatrix} 1 & 0 \\ 0 & \frac{n_i}{n_j} \end{bmatrix} \tag{4.2}$$

Here, n_i is the refractive index from which the beam exits and n_j is the refractive index of the material to which the beam enters.

The GRIN fiber: The ABCD matrix of a GRIN fiber is given by

$$\begin{bmatrix} A & B \\ C & D \end{bmatrix} = \begin{bmatrix} \cos(gl) & g^{-1}\sin gl \\ -g\sin(gl) & \cos(gl) \end{bmatrix} \tag{4.3}$$

with $g = \frac{2\pi}{\Lambda}$, $\Lambda = \frac{2\pi a}{\sqrt{2\Delta}}$, l is the GRIN length, and $\Delta = \frac{(n_1 - n_2)}{n_1}$. n_1 and n_2 are the refeactive indices at the core center and the edge of the core respectively as discussed in Sec 2.2.1. The refractive indices n_1 and n_2 were not provided by the manufacturer and were taken from [18] , for the calculations $n_1 = 1.483$ and $n_2 = 1.453$ were used.

Step refractive index fibers: The step index fiber in this case can be assumed as a spacial mode filter that transports the light entering the fiber along the whole fiber length with a fixed MFD. Assuming the light entering the step index fiber to be Gaussian and neglecting the losses for a very short length of the fiber, The ABCD matrix for propagation as such is given by,

$$\begin{bmatrix} A & B \\ C & D \end{bmatrix} = \begin{bmatrix} 1 & \frac{d}{n_i} \\ 0 & 1 \end{bmatrix} \tag{4.4}$$

Here, n_i is the refractive index of the medium.

4.1.2 Corrections to the model

This model was improved by including the other perturbations such as the effect of splicing and the effect of shooting as discussed below.

Splice overlap region: The model gave consistently a tighter focusing of the beam than what was observed, suspecting the splicing of the SM-GRIN fibers could have an effect on this, a layer of fused region corresponding to the length of SOR as mentioned in 3.1.2 was included. The refractive index for this layer was taken to be the mean refractive index of the SM part and the GRIN fiber part. This introduces two more interfaces and the propagation in this part is similar to the propagation inside a step index fiber. This addition of the SOR in our model resulted in a more closer propagation results compared to our observations.

Spherical end facet: We also observed that the beam propagation is hugely affected by the spherical end facet after shooting as shown in Fig 3.12. We suspected the spherical surface affected the divergence angle of the out coupled light. So the ABCD matrix for a spherical surface was included in

the model and is given by,

$$\begin{bmatrix} A & B \\ C & D \end{bmatrix} = \begin{bmatrix} 1 & 0 \\ \frac{n_i/(n_j-1)}{ROC} & \frac{n_i}{n_j} \end{bmatrix} \tag{4.5}$$

Here, n_j is the refractive index of the GRIN and n_i is the refractive index of Air. By replacing the interface matrix between free space and the flat end facet of the GRIN fiber; by the spherical interface. We got better matching of out results to our observations. Here, we used the mean refractive index of the GRIN fiber for simplicity.

4.1.3 ABCD matrix for SM-GRIN assembly

The input q parameter on our case is the beam at the end of the SM fiber. Assuming the out coupled beam from a SM fiber has the focus at is at its end facet, the input ray q parameter q_{in} can be written as $q_{in} = iz_0 = \frac{\pi n_{SM} w_0^2}{\lambda}$ as discussed in 2.1.2. Here n_{SM} is the refractive index of the SM fiber, w_0 is the waist radius at focus and $\lambda = 780$ nm. This beam then hits the interface between SM and the SOR, propagates through SOR and hits the interface between SOR and GRIN fiber; Propagates through the GRIN and has the spherical end facet in the place of the interface between Grin fiber and the free space(Air in our case). Thus cumulative matrix is written as,

$$\begin{bmatrix} A & B \\ C & D \end{bmatrix} = \begin{bmatrix} 1 & 0 \\ \frac{n_g-1}{ROC} & n_g \end{bmatrix} \begin{bmatrix} \cos(gl) & g^{-1}\sin gl \\ -g\sin(gl) & \cos(gl) \end{bmatrix} \begin{bmatrix} 1 & 0 \\ 0 & \frac{n_g}{n_m} \end{bmatrix} \begin{bmatrix} 1 & \frac{d}{n_m} \\ 0 & 1 \end{bmatrix} \begin{bmatrix} 1 & 0 \\ 0 & \frac{n_m}{n_s} \end{bmatrix} \tag{4.6}$$

Using this matrix in Eqn 4.1 the output q parameter of a Gaussian beam passing through assemblies can be calculated. Using this formalism the Refocusing length of the SM-GRIN assembly is calculated.
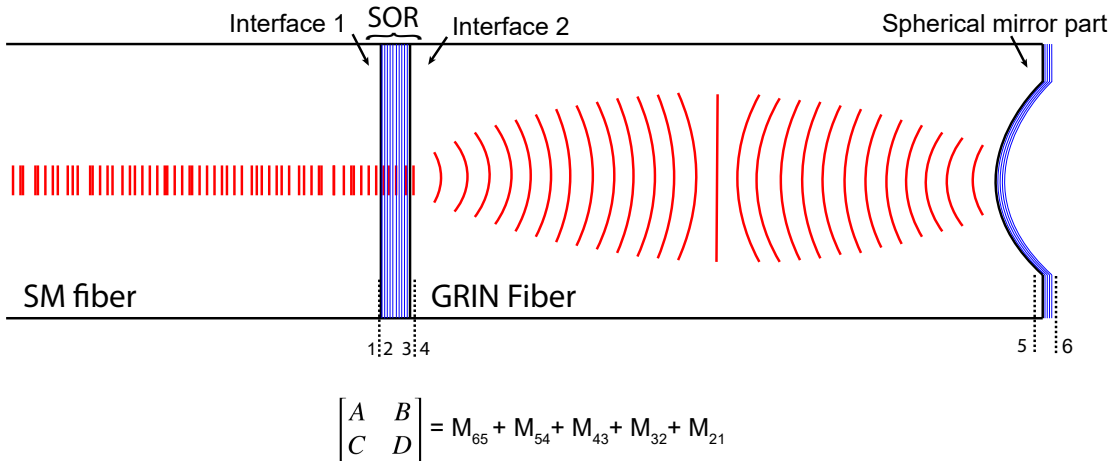

Figure 4.1: This figure gives the overview of the different optical elements the incoupled Gaussian beam propagates through and how the final cumulative matrix is calculated
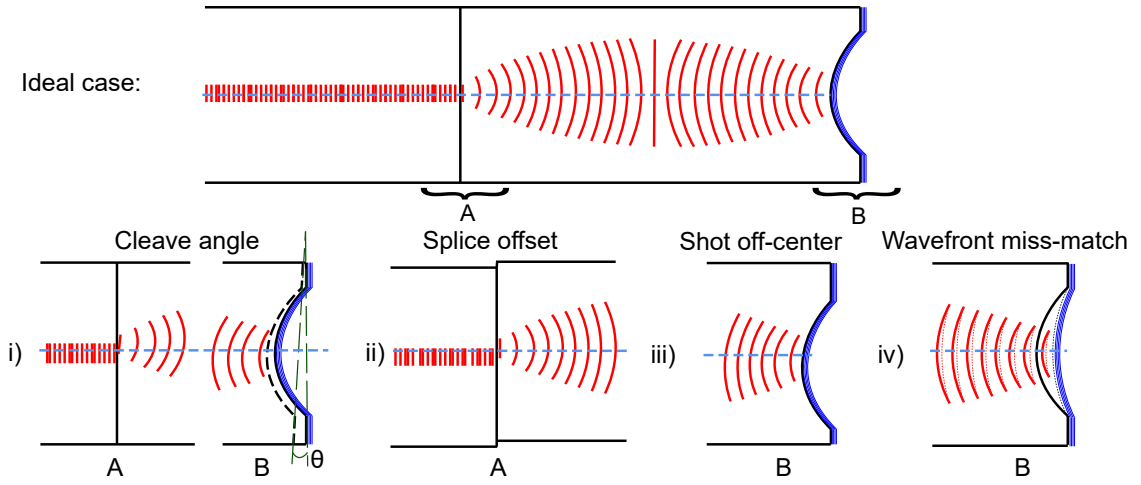
Figure 4.2: This figure gives the overview of the possible fabrication imperfections that can occur. The wave fronts of the Gaussian beam inside the assembly is shown in the upper figure. The effects of the imperfections are pronounced in the two regions A and B highlighted. In sub-figure i) we see the effects of the cleave angle θ The wavefron gets deflected and is not coupled into the SM fiber. In sub figure ii) we see the effect of the splice offset where the light is not efficiently coupled back to SM fibers. In sub figure iii) we see the effect of Shot offset, here the wave front gets deflected similar to cleave angle error. In figure iv) we see the effect of having the mismatch in wavefront and the ROC affecting the backward propagation

4.2 Analysis of assembly fabrication imperfections

After our first attempt of the coating run (see Sec 5.1), we tested the fiber assemblies for the back reflection from the coated mirror part of the end facet, this was done by coupling polarised light into the fiber, when the light hits the mirror that polarisation is shifted by $180°$ this beam is then passed through the polarisation beam splitter and its power is measured using the photo diode. The schematic of this is shown in the Fig 4.3. The fibers were coated with low transmission mirrors of 10 parts per million (ppm) so we expected to see more than 90% of the light to be reflected back but we observed that there was less than 6% back reflected.

This could be because of the fabrication imperfections. First, the end facets had cleave angles which redirected the reflected beam path away from the SM core resulting in loss of coupling. Second, there could be splice offset between the SM fiber and the GRIN fiber at the splice point leading to a reduced coupling of the reflected beam into the SM fiber. Third, the shot offset of the spherical structures with respect to the axis of the assembly and Fourth, a miss match in the ROC of the wave front and ROC of the shot fiber. These can be visually be understood from Fig 4.2. We also theoretically analysed these effects using the ray transfer matrix formalism. This was done by checking the overlap between the forward propagating beam and the reflected beam using the Eqn 4.7 taken from [22].

$$\tau_0 = \frac{2}{[(\overline{\omega_0}/\omega_0 + \omega_0/\overline{\omega_0})^2 + (2/k\overline{\omega_0}\omega_0)^2 s^2)]^{1/2}} \tag{4.7}$$

In this equation ω_0 and $\bar{\omega}_0$ are the waists of two different Gaussians and $s = \bar{z} - z$, wit z and $\bar{z}$ the positions of the beam.
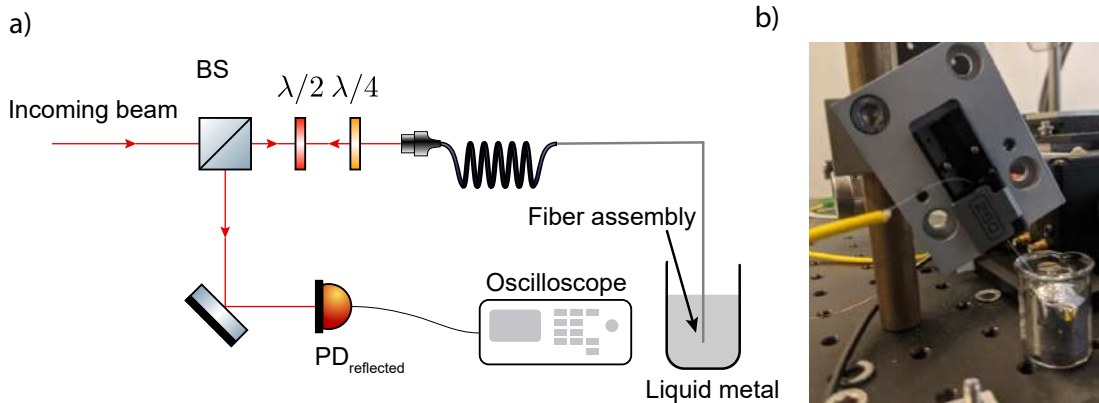
Figure 4.3: a) shows the setup used to characterize the effects of fabrication imperfections in the setup.Light is coupled into the SM GRIN fiber assembly and it is dipped into liquid metal, this acts as a reflecting medium that can reflect the light back into the assembly, The reflected power is read using the photo diode. b) is the image of an assembly dipped into the liquid metal

4.2.1 Effects of cleave angle

The analysis for the cleave angle effects were done by checking the coupling efficiency (overlap) of the forward and backward propagating beams for different GRIN lengths with cleave angles as a variable. The results are as shown in the Fig 4.4. We observe two distinct peaks at $250\,\mu m$ and $500\,\mu m$ where the coupling efficiency is maximum. The gradient gives the change in the cleave angles. A closer look at the gradient for GRIN length of $250\,\mu m$ (half refocusing length of the GRIN fiber) reveals that the coupling drops rapidly with increasing cleave angles where as at $500\,\mu m$ (full refocusing length) the change is less.

The results of the simulations can be explained with Fourier transform model of the light beam at focus of the lens as as shown in Fig 4.5, the grin fiber at half of the refocusing length is analogues to the 1f- 1f Fourier transform system of a lens where, the focused beam on the real image plane x propagates through the lens and reaches the Fourier plane x' this beam at the Fourier plane has the wave vector parallel to the optical axis. A cleave angle in the endfacet of out GRIN fiber can be considered as a tilt in the wave vector in the Fourier plane which when propagated back the beam gets focused transversely away from the initial focus position in the real plane. Similarly the GRIN fiber at full refocusing length is analogus to the same system with two lenses separated by twice the focal length. In this case the focused beam propagates through two lenses to reach the real plane x'' where beam is focused again and any small tilt in this axis does not have a huge effect in the wave vector when propagates back. With this we can see how the cleave angles at the end facets affects the reflected beam and are critical for the back coupling.

In order to build mode matched cavities the GRIN lengths have to be between $250\,\mu m$ and $350\,\mu m$ where we get the optimum mode size at endfacet and we can better shape the beam profiles. Hence the techniques have to be improved to cleave fiber with small cleave angles.

The experimental characterization of the cleave angles were done by fabricating assemblies of
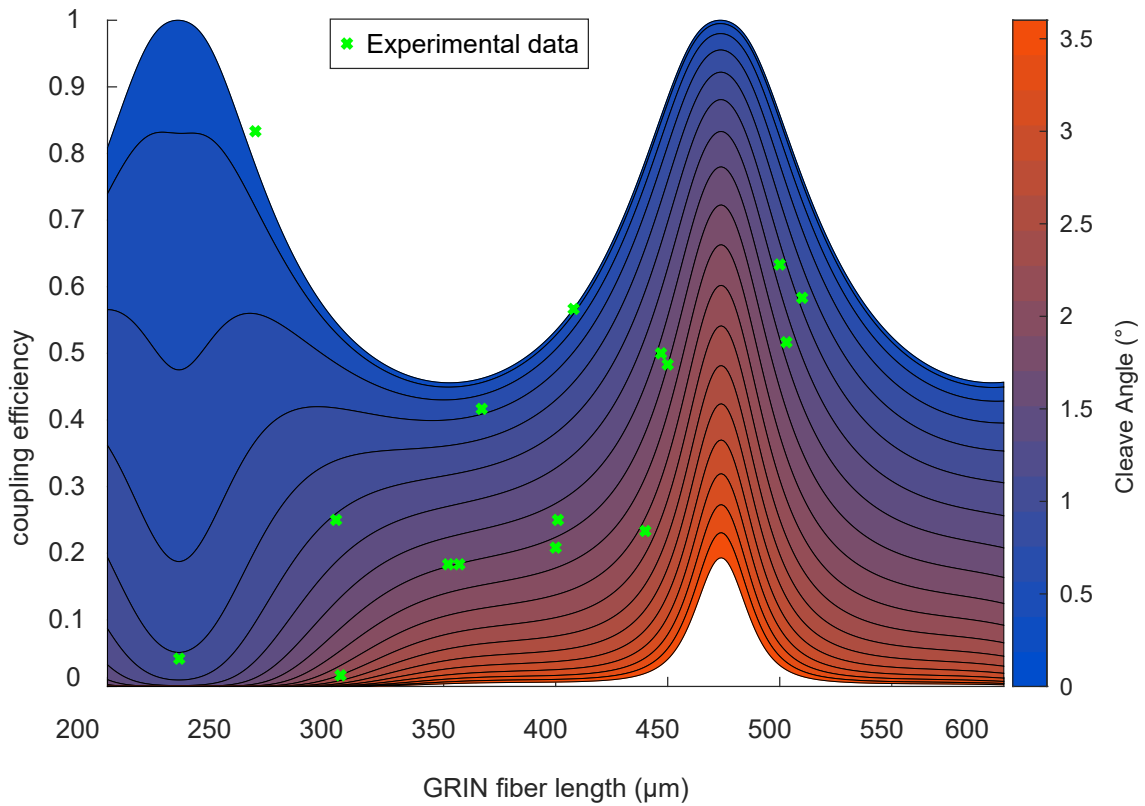
Figure 4.4: This figure shows the effects of the cleave angle at the end facet of the fiber assemblies. Here the coupling efficiency is plotted for different GRIN lengths with different cleave angles. The gradient in the figure corresponds to various cleave angles on the fiber end facet. We can observe two distinct bumps on the plot, the first one at around 250 μm of the GRIN fiber length corresponds to half of the refocusing length of the GRIN fiber and the second bump at around 250 μm of the GRIN fiber length corresponds to a complete refocusing length of the GRIN fiber. The green points in the figure are the experimentally measured backreflected powers normalised to the power backreflected signal of SM fiber.

different GRIN lengths and dipping them in liquid metal (Galinstan) as shown in Fig 4.3. The liquid metal acts as the mirror coating and reflects the light beam inside the fiber assembly fiber. The measurements were normalised with respect to a measurement with a cleaved bare SM fiber with which we expect to see the maximum back reflection. The results of experimental data is also plotted with the simulations. These data points indicate the coupling efficiency of all the fabrications included and do not just represent the effects of cleave angles. However, as cleave angles have the maximum effect on the backreflected signal we compare it with the simulations to get a context about the scale of cleave angles we have in our assemblies and are between 1 and 2 degrees.
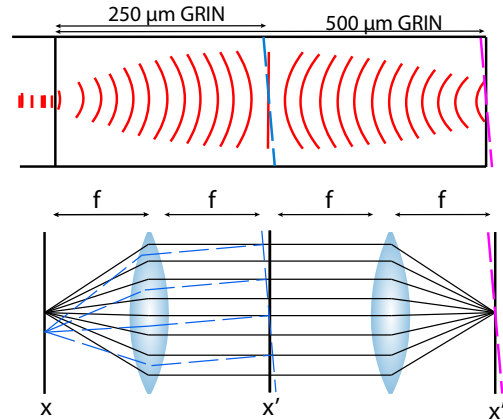
Figure 4.5: This figure gives a visually intutive explanation on why the cleave angle has large effects at half refocusing length of the GRIN fiber and less effects on full refocusing length.

4.2.2 Effect of splice offset

When the axis of the SM fiber with respect to the axis of the GRIN fiber is off, the light beam does not couple back into the SM fiber efficiently because of the small core diameter of the SM fiber. We have seen the working of the splicer in Sec 3.1.2. The parameters used to splice the SM GRIN fibers were optimised by David Röser in his masters thesis [11].Fig 4.6 shows the effect of splice offset in the coupling efficiency of the reflected beam. The gradient in colors represent the change in splice offsets from 0 to 1 micron. We observe that the coupling efficiency is sensitive to splice offsets to less than 1 micron. The splicer reports an error if the axis offsets are more than a set threshold but the technique with which it measures the offset is unknown. Moreover, these offsets cannot be measured with the microscopes that we use, as they have an error of 1 micron. Hence this remains one of the parameters that cannot be characterised with the current setup.

4.2.3 Effect of Shot offset

Spherical end facets in our fibers are produced by laser ablation process which was discussed in detail in Sec 3.4. One of the challenges faced during the fabrication was the pointing stability of this laser beam. As the beam kept deflecting in the order of few microns every 20 minutes due to the thermal instability, we were not able to consistently shoot exactly at the center of the fibers, this produces off centred shots, which primarily affects the alignment in the cavities but also has a huge effect on the back reflection. The beam propagating through the GRIN fiber reflects back in the same beam path only if the wavefront matches the ROC of the spherical mirror, if the Spherical surfaces are off centered, this reflects the wave with a small angle similar to the effect of cleave angle in Sec 4.2.1 and hence the reflected beam gets deflected and focused back away from the SM core and cannot couple into the SM fiber.

The back coupling efficiency can also be simulated using the ray transfer matrix formulation and similar to Sec 4.2.1 using Eqn 4.7 we can check the coupling efficiency of the reflected beams. The results are shown in Fig 4.7 and we can observe that the off centred shots have a greater effect again

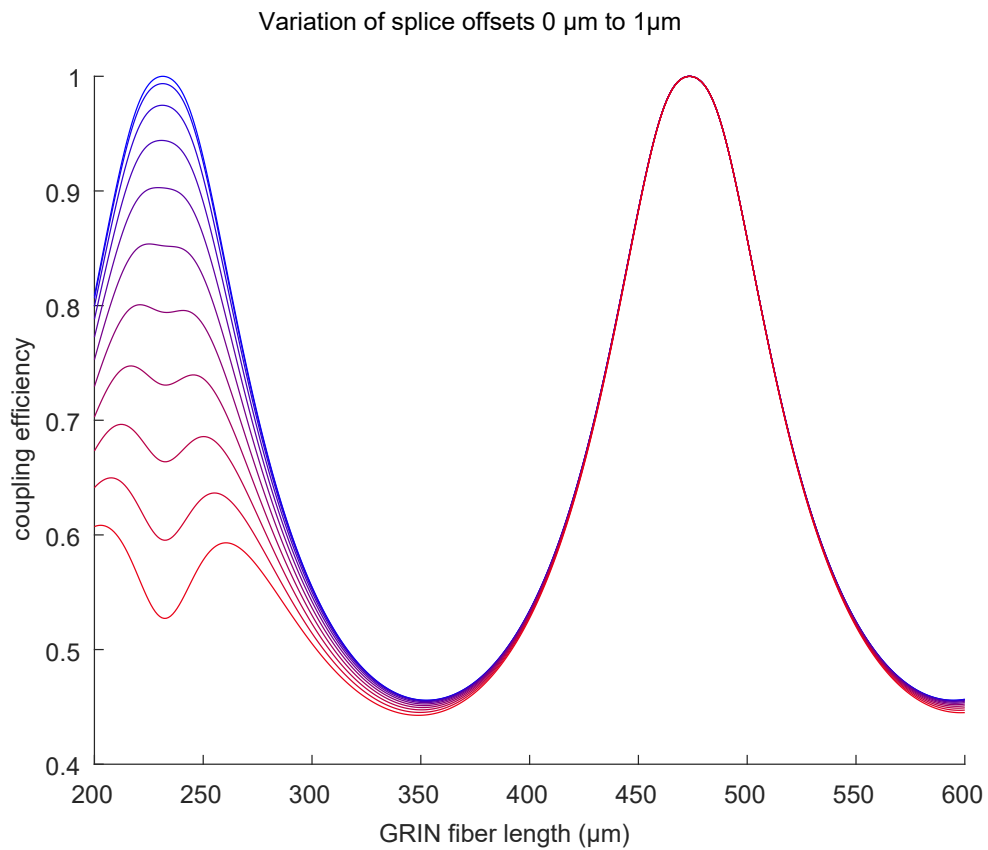Figure 4.6: This figure shows the effects of the splice offset between the SM GRIN fiber. The gradient in the lines corresponds to the variation in splice offset changing between 0 and 1 micron. we can see the coupling efficiency has large effects for GRIN lengths around 250 μm where the beam at maximum expansion inside the GRIN fiber similar to cleave angle effects and recovers at the full refocused part of the GRIN fiber.
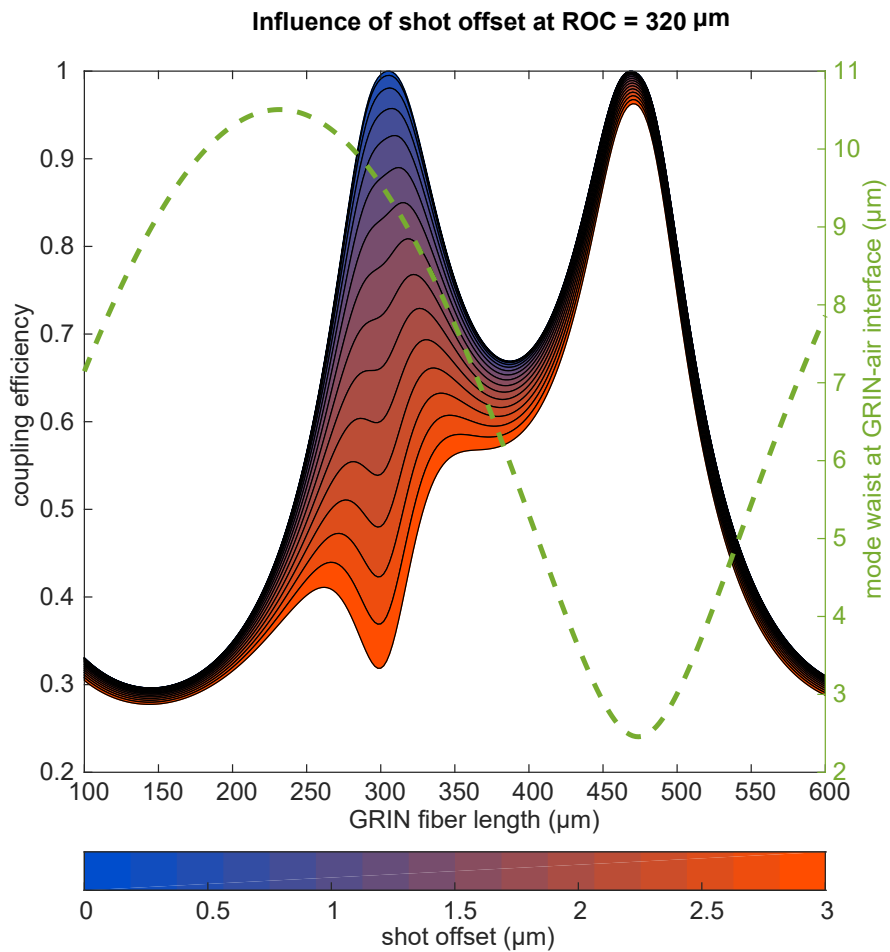
Figure 4.7: This figure The coupling efficiency is plotted for shot offsets varying from 0 to 3 microns, for various GRIN lengths, The mode waist of the light beam inside the GRIN fiber is also shown in the dotted grin line. Similar to the previous effects the coupling is sensitive at 250 μm GRIN fiber lengths.

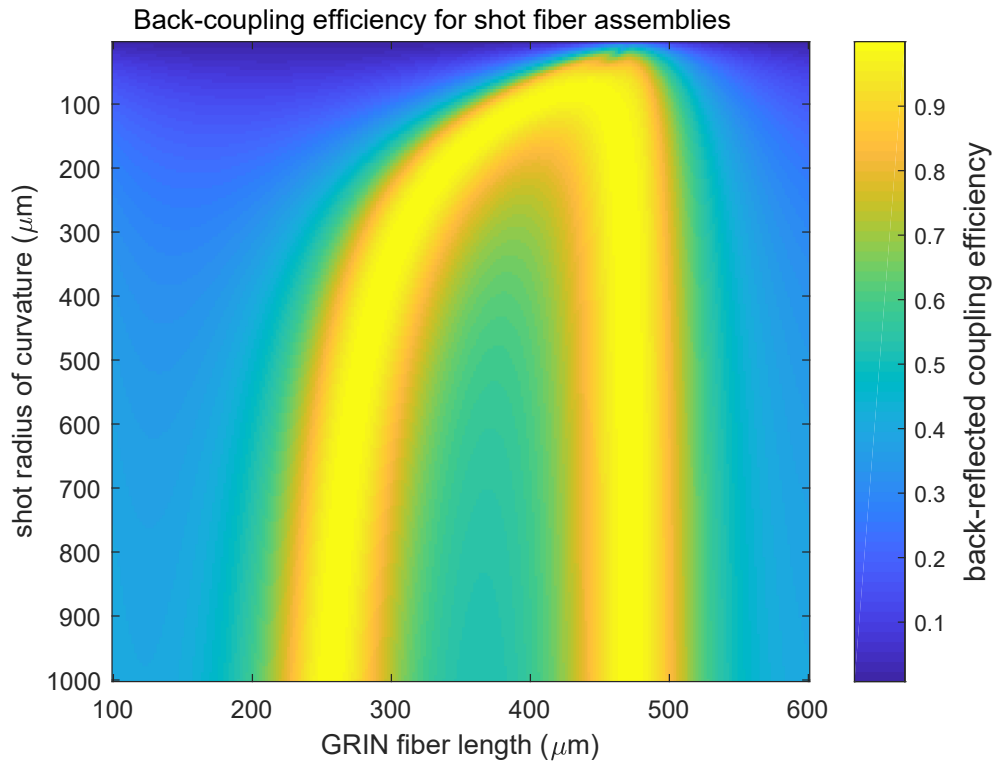Back-coupling efficiency for shot fiber assemblies

Figure 4.8: This figure gives the back reflected coupling efficiency for different ROC shot on the fiber end facet. This is used as a reference to decide what ROCs are shot corresponding to the GRIN lengths used.

at half of the refocusing length of the GRIN fibers similar to the effect of cleave angles and has lesser effect at the ful refocusing length. The coupling also varies with shots with different Radius of Curvatures (ROCs) at the end facets. We observe the coupling efficiency of the shot offsets are sensitive between $250\,\mu m$ and $300\,\mu m$ GRIN lengths which is the GRIN lengths we use in our assemblies.

4.2.4 Effect of Wave-front miss-match

The wave vectors of the Gaussian beam has to be incident perpendicularly to the end facet of the mirror for it to reflect back to the SM fibers with the same beam path as the incoming beam. This is not possible if the ROC of the wavefront does not match with the ROC of the spherical surface shot at the end facet of the assemblies. This miss match causes the beam to expand more when reflected and not couple back into the SM fiber efficiently. Fig 4.8 gives the results fot the effect of wavefront miss match in the assemblies. The coupling efficiency is plotted for different shot ROCs ablated on assemblies with different GRIN lengths. We can also observe that the coupling improves drastically for a given GRIN length when the ROC shot is small and saturates quickly for larger ROCs. As it is easier to produce ROCs larger than $400\,\mu m$, and also using larger ROCs decreases the effects of shot offsets, we started to shoot larger ROCs in the final coating runs.

4.3 Mode matching Analysis

In this section we analyse the overlap of the cavity mode and the outcoupled Gaussian mode. From Sec 2.1.2 by using Eqn 2.4 the waist at the mirror end facet can be calculated for a given cavity length. Using this and by simulating the outcoupled light from the fiber assembly the overlap between the cavity cavity mode and the light mode can be calculated. The results of this analysis is shown in Fig 4.9. For a cavity length of $L_{cav} = 300\,\mu m$ the overlap is shown for varying GRIN lengths and varying ROCs. We can observe that the ROC in the end facets have very less impact on the overlap for values larger than $300\,\mu m$ (for a constant GRIN length).
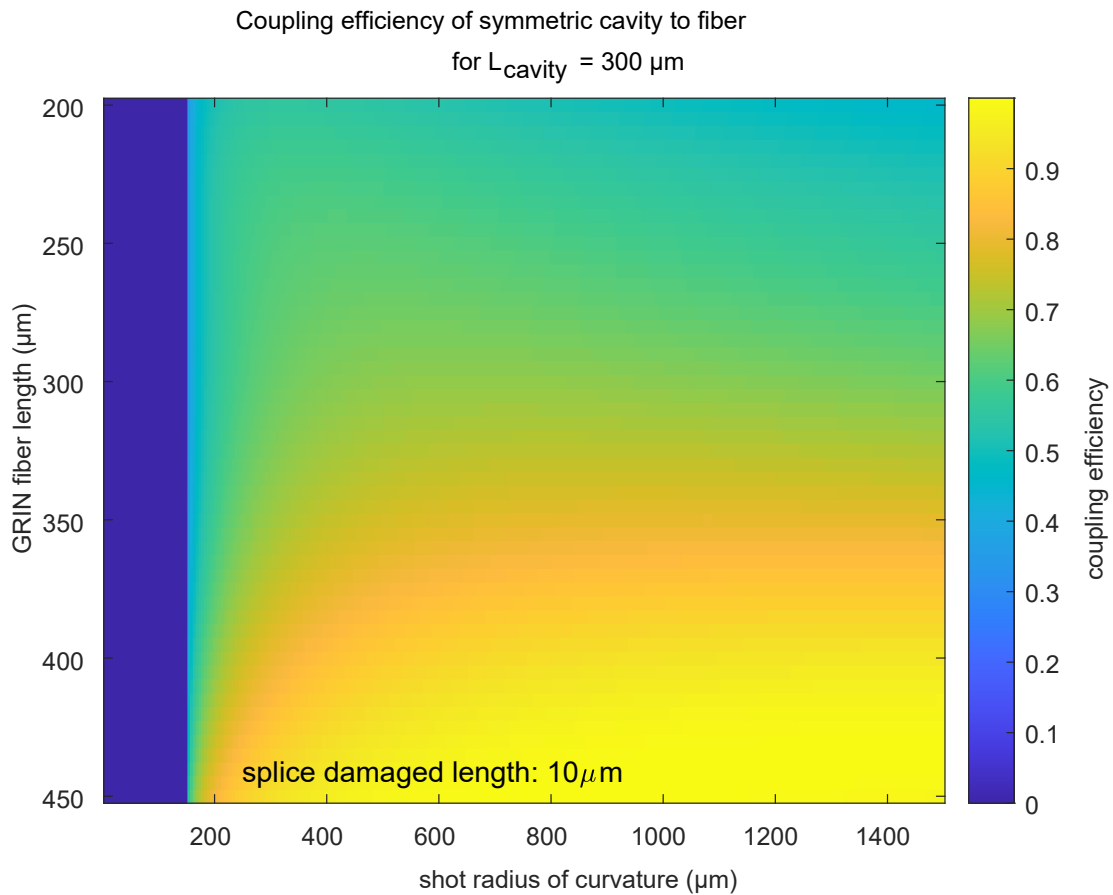

Figure 4.9: This figure gives a map of the overlap between cavity Gaussian field and the Gaussian beam out coupled from the assembly for various GRIN lengths and ROCs
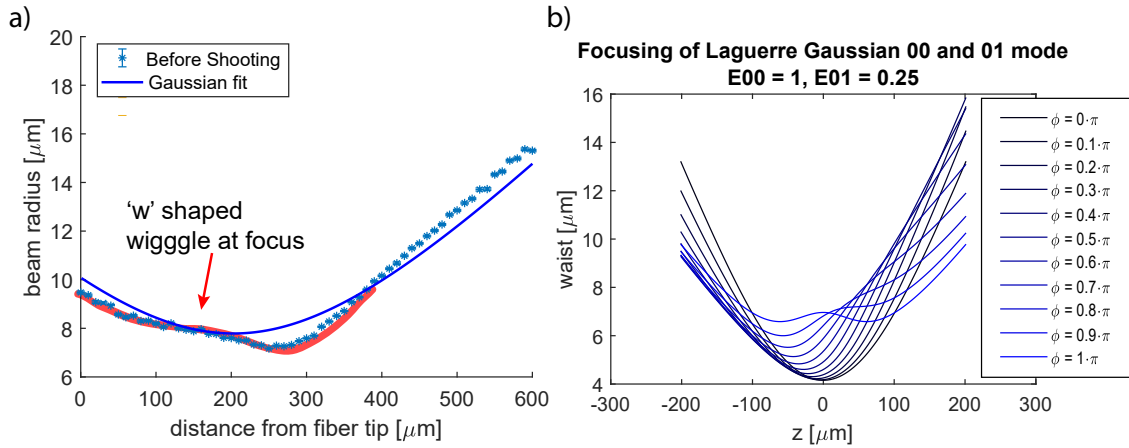
a)

b)

Figure 4.10: a) shows the output propagation of a shot SM GRIN assembly, the 'w' shaped wiggle deviating from the gaussian propagation fit is highlighted in red. b) gives the results of the simulations with higher order Gaussian beams. We were able to see a similar 'w' shaped wiggle when there is a phase shift between the fundamental mode and first higher order mode

4.4 Beam propagation simulations

We observed that the propagation of the out coupled beam was not purely Gaussian and had deviations at the beam focus. We observed over several assemblies that near the focus of the beam a 'w' shape, as highlited in Fig 4.10. This effect was pronounced after the laser ablation process. In order to understand the cause of this discrepancy we simulated propagation of the out coupled beams, our suspicion was an additional Gaussian beam with a significantly low electric field produced from the second reflection of the light through the GRIN fiber happening at the splice point.

Two out coupled Gaussians: Our first approach was to simulate a case where there are two superimposed Gaussian beams outcoupled from the fiber assembly, for this we started by first simulating the electric fields of two ground Laguerre Gausian modes E_{00} in X-Y planes in $10\,\mu\text{m}$ length intervals in Z axis and summed them together. This was done with the different beam waists w_0^1 and w_0^2 of the two beams, different waist positions of the beam waists z_0^1 and z_0^2, and different electric field strengths of each beam E^1 and E^2 of both the beams, and also introducing a phase difference $\delta\phi$ between them and the total intensity of the electric fields were calculated. In order to reduce the size of the data set, these summed electric fields in each plane were fit using 2D Gaussian beams and the waist of the beam at each plane was calculated similar to our experimental characterization in Sec 3.2.3. The results are shown in Fig 4.10, we were not able to reproduce the 'w' structure at the focus. We suspected this could be an effect of a higher order modes in the out coupled beam.

Higher Order modes: As we did not see similar results as we observed while simulating two ground Gaussian modes, in the next step we superimposed the ground Gaussian mode to the first order mode. As we observed a smooth intensity profile without any splitting we used the first azimuthal higher order mode E_{01} instead of the E_{10} mode. Similar to the other simulation we had the waist position z_0

waist size w_0 the Electric field strengths E and a phase difference between them as variable parameters ans we simulated the intensities of the summed electric fields, for them with Gaussians and plotted the beam radius along the propagation. The results are shown in Fig 4.10, we were able to reproduce this 'w' wiggle using the first order Laguerre Gaussian mode for an electric field of about 30% of the ground mode which accounts to a very tiny fraction of the higher mode. As this effect could be due splice imperfections and is not very consistent with all assemblies of same parameters, this could be only useful if we fit the out coupled beam with this superimposed beam. As this has a huge parameter space of seven variables and had to fit a the Laguerre Gaussian Function, it takes several hours to fit every beam propagation with it. As this information was not very crucial for our results we conclude this analysis by saying this anomaly is due to the presence of a low intensity E_{01} in the out coupled beam.

Building and Characterizing FFPCs

In this chapter we present the details about fabricating, packing and sending a large number of fiber assemblies for coating the dielectric mirrors at the end facets. We present the process of assembling a cavity using the coated fiber mirrors. We compare them with another cavity built using bare SM fibers and see if we have improved the mode matching in the cavities.

5.1 Three coating Runs

The laser ablated end facets must be coated with a reflective material in order to produce cavities with good finesse. Even though metallic coatings are easier to produce, in order to get high finesse, several layers of dielectric materials like Ta_2O_5 and SiO_2 with a thickness of $\lambda/4$ of the wavelength of the light used are applied on the end facets. These layers form a Bragg mirror, using this techniques high quality mirrors with transmitivity (T) as low as 10 ppm can be coated on the end facets . The coating of the mirrors on the endfacets were outsourced to 2 companies, Layertek Gmbh and LaserOptik Gmbh.

During my master thesis we sent 3 batches of fiber assemblies for coating. For the coating to be successful the fibers and the holders that are used have to be kept clean. To achieve this the fiber assemblies were fabricated in clean room conditions and coper coated fibers were used as the fibers are coated for vacuum compatability. The precise deposition of dielectric material can be implemented via ion-beam sputtering, a widely used technique that has so far provided the macroscopic mirrors with lowest amount of losses. For this endfacets of the fiber assemblies have to be placed perpendicular to the sputtering beam of dielectric layer to be coated. The holders should also be accessible to store and retrieve fibers for testing, for this we designed coating disks in cooperation with both the companies. These coating disks can house the home designed fiber holders that can store 26 fibers and are compatible with the Laser ablation setup Sec 3.4 that we use. The image of the coating disk used and a fiber holder containing the fibers is shown in Fig 5.1.

In our first attempt we fabricated SM GRIN fiber assemblies of desired GRIN lengths. These fibers were placed in the fiber holder and the endfacets are ablated with desired ROCs and the fibers were directly packed in clean room conditions and were shipped for coating. The assemblies were coated with mirrors of 10 ppm transmission. In this coating in addition to assemblies a few bare SM fibers with spherical end facets and a few mirror substrates for our reference. When we got them back we

Figure 5.1: a) is an image of one of the coating disks used for coating dielectric mirrors on fibers, several fiber holders placed perpendicular to the coating disks and the fiber tails are fiddled around the disk and are clamped. b) is an image of one of the home built fiber holder that can store the fiber assemblies produced. The fibers are held in place by the clamping springs in each grove.

observed that more than 90% of the assembly mirrors had only about 10% of light reflecting back as mentioned in Sec 4.2. The forward propagation was also distorted for most of the fibers. This could have happened because of fabrication imperfections or the holders could be damaged during transportation. We observed the other bare SN fibers did not have these issues. Here we realised that the forward propagation has to be characterized for every fiber before and after shooting in order to understand the probable fabrication imperfections that affect the beam profile. At this point we started the back reflection characterization and characterizing the fabrication imperfections discussed in Sec 4.2.

After characterising the possible fabrication imperfections and simulating the effects of these imperfections on the beam propagation, we prepared the second and the third coating runs, for this the beam profiles of every assembly before and after the laser ablation process was characterized to quantitatively characterize the results. Improvements to the design of fiber holders to secure the fragile part where the copper coating was removed were done and the perimeter of the coating disks was sealed to prevent any dust entering the disk. The assemblies were coated with mirrors of 2000 ppm transmission for the second coating run. When we got back the coated mirrors, we observed the forward propagation of the fibers from the second coating run remained the same compared to the propagation before coating indicating that the coating was successful.

We prepared and sent about 150 fiber assemblies for coating through the three coating runs. We started to build cavities from the coated mirrors. In the next section we will discuss the fabrication and characterizations of the FFPCs using the coated fiber assembly mirrors.

5.2 Cavities with coated fibers

The fiber mirrors are are tested for back reflection and forward propagation before building a cavity using them. The forward propagation has to remain the same before and after propagation only these mirrors are selected for building cavities. These mirror surfaces have microscopic imperfections from the sputtering of the dielectric mirrors, in order to smooth out the surface the fibers go through a process called annealing. The fiber mirrors are placed in the oven at about $300^{\circ}C$ for 3 to 5 hours. Once the fibers are verified for forward and backward propagation, and annealed they can be used to build cavities [23].

5.2.1 Building Cavities

The fiber mirrors are placed in V-grooves that are connected to 3 axis translation stages and two axis angular tilt stages. By iteratively adjusting the translation stages and the tilt stages, the mirrors can be aligned and a cavity is assembled [19]. The characteristics of these cavities are extremely sensitive to the alignment of the fiber mirrors. The alignment can be can be simplified by using a technique developed by one of our PhDs Carlos Saveda, where a ferrule of a fixed bore diameter can be used[24]. Fiber mirrors can be inserted into these ferrules where the fibers are guided and are self aligned inside the bore of the fiber Fig 5.2.
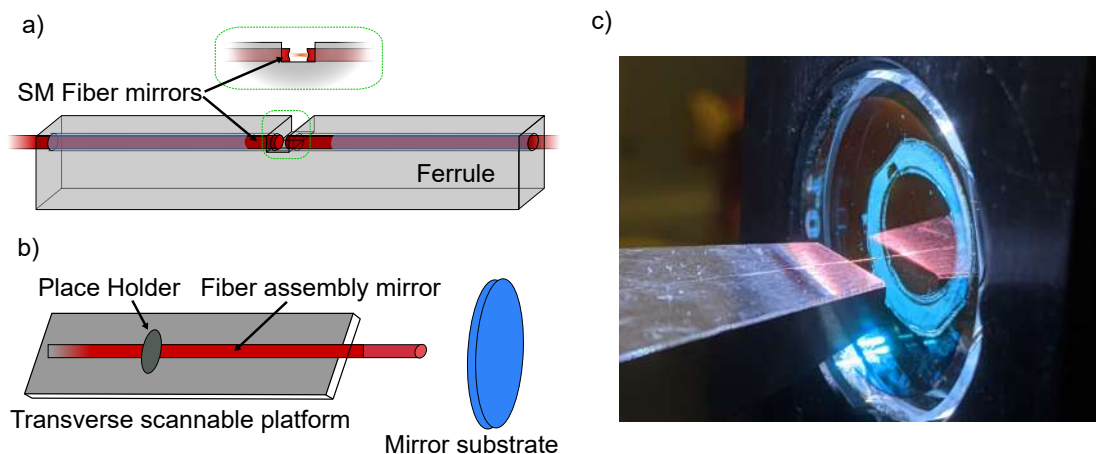

Figure 5.2: a) shows a blueprint of two bare SM fiber mirros that are guided inside the bore of the ferrule The ferrule has a slit that is grounded half way through it. This gives us access to the cavity and helps in cleaning the cavity and the fiber mirrors. b) shows the blueprint of an asymmetric cavity that was built using a SM GRIN fiber assembly mirror in one end of the cavity and a flat mirror substrate on the other. The flat substrate is placed in angular tilt stages and the fiber assembly sits on a 3 axis translation stage c) is an image of an asymmetric cavity built with SM GRIN assembly and a flat mirror substrate.

We built two types of cavities, a symmetric confocal fiber cavity with two single mode fiber mirrors shot with same ROC on both sides and an asymmetric hemispherical cavity with a fiber mirror of known ROC as one of the cavity mirrors and a flat mirror substrate as the other mirror as shown in Fig 5.2. The symmetric cavity was built using bare SM fiber mirrors and the asymmetric cavities with

SM GRIN assembly mirrors. This was done to draw a comparison between FFPCs built with bare SM fibers and FFPCs built with SM GRIN assembly mirrors.

Symmetric cavities : The symmetric cavity was built using bare SM fiber mirrors of old coating runs that had 200 ppm coatings and mirrors with same ROC of 170 μm. These mirrors were chosen because several cavities have been built using these fibers by Carlos Saaveda and have been well studied [24], hence they can be used as a good baseline to compare the cavities built with fiber assemmblies.The schematic of fiber mirrors forming a cavity is as show in Fig 5.2. Here a ferrule of bore diameter of 130 μm is used. The bare single mode fibers are guided through the bore of the ferrule. Due to the narrow bore diameter the fibers self align with respect to each other and a cavity mode is produced between them. One end of the fibers is connected to a rotation stage to rotate the fiber along its axis to compensate for the polarisation splitting that happens in the cavity due to the residual ellipticity of the Spherical end facet [25] and can be observed in the reflection signal. The other end is connected to a scanable translation stage where a triangular pulse is applied to scan the length of the cavity.

Asymmetric cavities : The asymmetric cavities with SM GRIN assembly mirrors of 10 ppm transmission. We built an asymmetic cavity because if its simplicity of alignment in free space; as were not able to properly align the fibers inside the ferrule. A schematic of asymmetric cavity is shown in Fig 5.2. For this both the Fiber assembly and the substrate were coated with mirrors of 10 ppm transmission and the assembly has a GRIN length of 316 μm and was shot with a ROC of 300 μm.

5.2.2 Cavity Characterization

To find the optical resonance of the cavity, one of the fiber mirrors is scanned using a piezo-driven translation stage while observing the cavity reflection of an incident probe laser. The blueprint of the setup used to characterize the cavity is as shown in Fig 5.3.

An infrared probe laser at 780 nm is passed through an Electro Optic Modulator (EOM) that can produce side bands at its driving frequency of ±250 MHz apart. This is sidebands are used as the reference frequencies to measure the linewidth and the finesse of the FFPC using the reflection signal. This beam with sidebands is passed through a beam splitter, a half wave plate and a quarter wave plate to control the polarisation mode splitting and is subsequently coupled into the fiber that guides it towards the cavity. The beam reflected from the cavity is coupled out and the reflected power is measured using the photo diode and can be observed using the oscilloscope. A triangular waveform is applied to the piezo-driven translation stage using the signal generation function of the oscilloscope in order to scan the length of the cavity. During the alignment process the reflection signal is continuously observed and the alignment is optimised to maximise the reflection signal and minimise polarisation splitting. The reflection signal is measured with the sidebands to calculate the finesse and without the EOM side bands to measure the coupling depths, for various cavity lengths.

The results of the measured reflection signal is as shown in Fig 5.4. This is the signal measured at 40 μm cavity length of the asymmetric cavity with a SM GRIN fiber assembly as one of the mirrors. We can observe the cavity resonance dip at zero detuning and the EOM side bands 250 MHz away from the resonance dip. The measured values are fit using a combination of dispersive function and
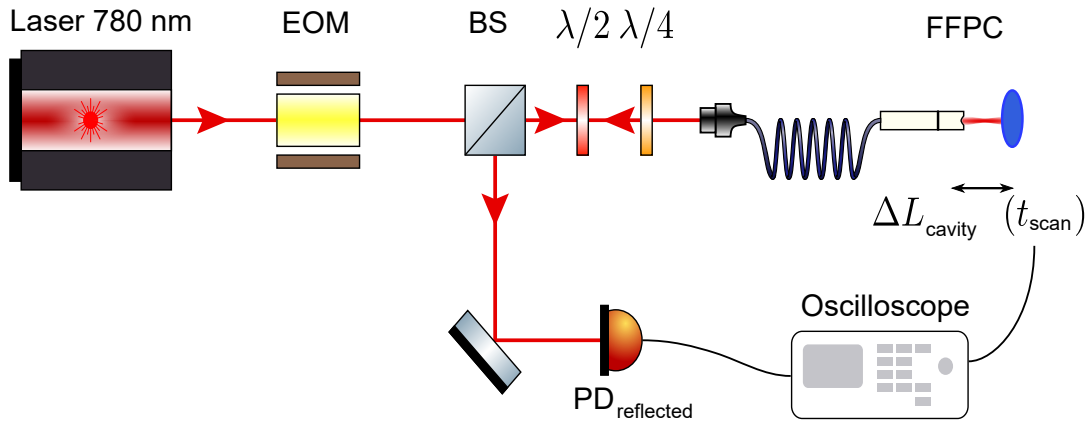
Figure 5.3: This figure shows the schematic used to characterize the FFPCs. The probe laser is passed through the electro-optic modulator EOM and is coupled into the fiber cavity. The reflection signal from the cavity is separated using the beam splitter(BS) and the power is measured in the photo diode. The length of the cavity is scanned using the piezo-driven translation stage. This figure is taken and modified from [24].

Lorentzian function [15]. Using this fit and reference from EOM sidebands the Finesse of the cavity can be calculated.

5.3 Results

In this section we present the results of the characterisation of both the cavities. We will compare the coupling depths we observe for these two cavities and look for improvement in the coupling depth for the asymmetric cavity where SM GRIN fiber is used. Finesse of these cavities are measured to check the onset clipping losses in the cavity of the cavity mirrors.

5.3.1 Symmetric cavity

For a symmetric cavity which has 20 ppm mirror coatings and ROC of $170\,\mu$m on both the mirrors, the finesse is shown in Fig 5.5 and coupling depth is shown in Fig 5.6 (on the left hand side). We see a finesse of about 80 000 for the cavity length up to $120\,\mu$m and it suddenly drops after $130\,\mu$m. This drop in finesse at $130\,\mu$m is exactly what we expect for a symmetric cavity of the given parameters. This orange curve is calculated using Eqn 2.7, this gives the expected finesse for the cavity parameters used and this agrees well with the measured results. Next, we show in Fig 5.6 a) the coupling depth of such a cavity. The red line shows the maximum coupling that can be expected for such a symmetric cavity. We were able to get a maximum coupling of about 55% for $30\,\mu$m cavity length and it gradually drops as we increase the length to more than $130\,\mu$m.
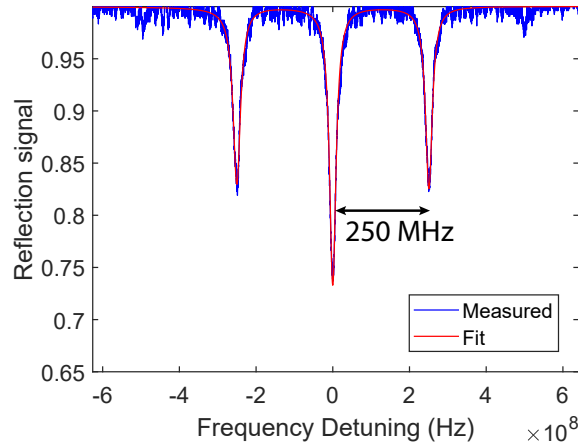
Figure 5.4: This figure shows the reflection signal when the EOM is turned on. The side bands 500 MHz apart can be observed aling with the resonance dip of the cavity and the light. A fit (red) to three equidistant Lorentzian curves provides the required frequency calibration to calculate the finesse. This is the signal measured at 40 µm cavity length of the asymmetric cavity with a SM GRIN fiber assembly as one of the mirrors.

5.3.2 Asymmetric cavity

Now we can compare the results of symmetric cavity with SM fiber mirrors to asymmetric cavities with SM GRIN assembly mirror. For mirrors coated with 10 ppm transmission, the finesse for this cavity is shown in Fig 5.5 and the coupling depth is shown in Fig 5.6 (on the right hand side). In Fig 5.5 b) we can see increased finesse up to 200 000. This is because of the use of high reflecting 10 ppm transmission mirrors. The measured finesse drops at 70 µm cavity lengths. Here the orange line shows the finesse we expect for a asymmetric cavity. We observe that, in our cavity the finesse drops for cavity lengths shorter than expected. This is because of our limit in the precision of aligning the cavity in free space. Fig 5.6 b) shows the coupling depth as the function of the cavity lengths. The orange line shows the maximum coupling we can get for a asymmetric cavity built with SM fiber. We observe a coupling depth of 70% compared to the 40% limit expected from the SM fiber at 50 µm cavity lengths. As we observe a higher coupling depth compared to the maximum limit expected from the SM fiber we can say the mode matching is improved for this cavity geometry. Here the coupling drops to less than 40% at 70 µm cavity length and this can also be associated to the limit in the precision of alignment of the cavity as we also see a drop in finesse at this length.

5.3.3 Discussion

The coupling depth of both the cavities at 40 µm cavity length is shown in Fig 5.7. We have achieved $\approx 70\%$ coupling using a SM GRIN assembly Fig 5.7 b) compared to 50% coupling when using a SM fiber Fig 5.7 a). This is possible because of the improved mode matching of the cavity mode and the light mode; therefore, more light gets coupled back into the SM GRIN fiber assembly from the cavity. This results indicate that using a SM GRIN assemblies higher coupling depths can be achieved.

Furthermore, it has to be noted that the coupling depth of 70% measured, is for an asymmetric
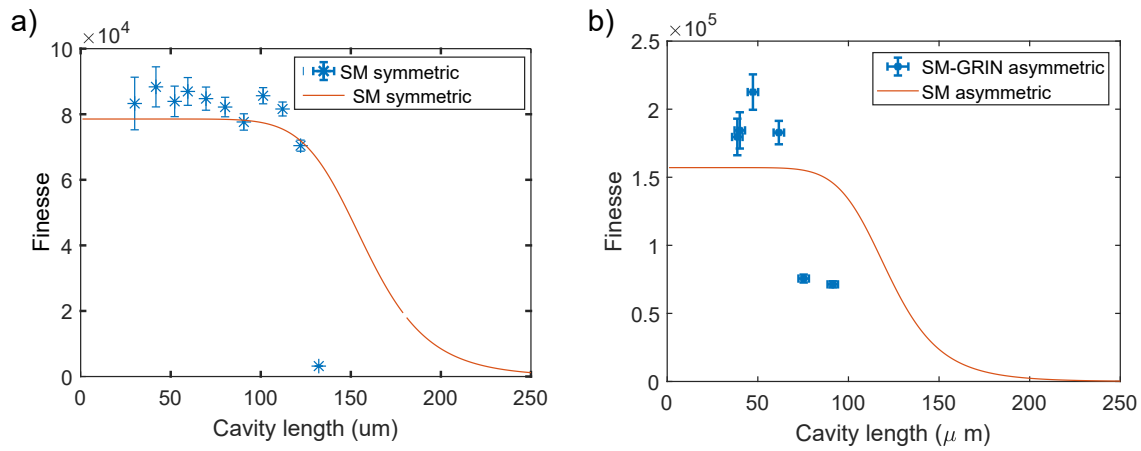
Figure 5.5: This figure shows the Finess of the cavity for different cavity lengths. a) shows the finesse of a symmetric cavity built using SM fibers of 20 ppm transmission. The orange curve shows the expected finesse and the blue data points show the measured values b) shows the finesse of a asymmetric cavity built using SM GRIN fiber assembly and flat mirror of 10 ppm transmission. The orange curve shows the expected finesse and the blue data points show the measured values

cavity. This is equivalent to having a 80 μm cavity with the same 70% coupling when a symmetric cavity is built with the SM GRIN assemblies with the same ROCs. By improving the alignment, one can build mode matched cavities of longer cavity lengths with improved mode matching.
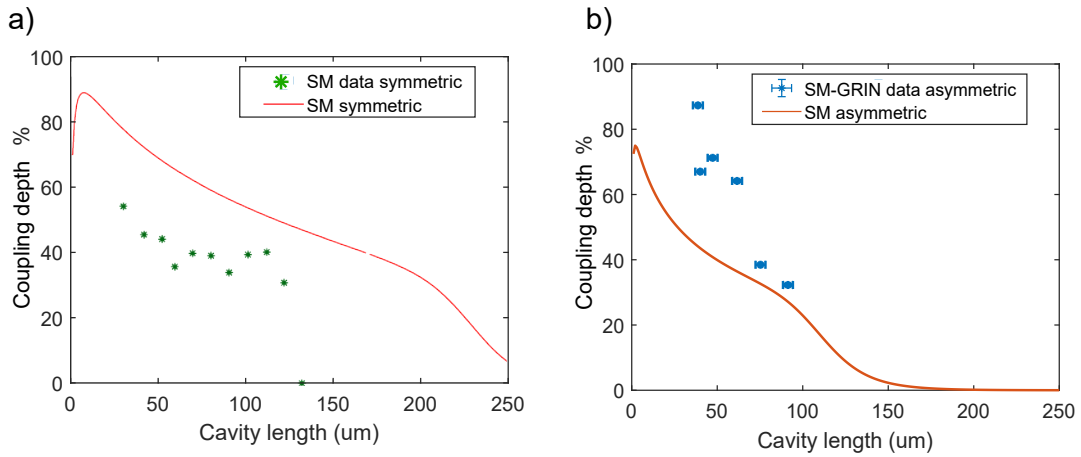
Figure 5.6: This figure shows the coupling depth of the cavity for different cavity lengths. a) shows the coupling depth of a symmetric cavity built using SM fibers of 20 ppm transmission. The red curve shows the expected coupling depth. a) shows the coupling depth of a asymmetric cavity built using SM GRIN fiber assembly and flat mirror of 10 ppm transmission. The orange curve shows the expected coupling depth
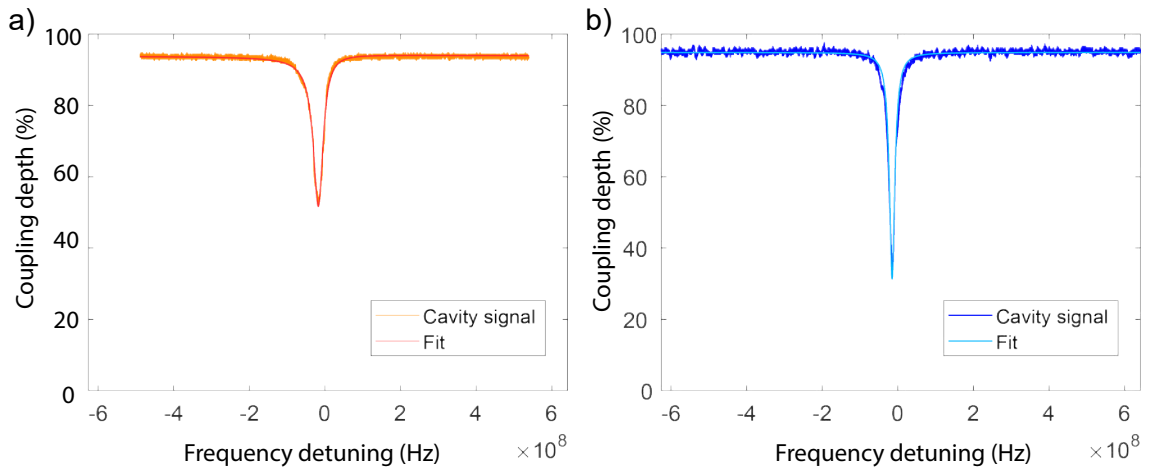

Figure 5.7: This figure shows the Reflection signal of Symmetric and asymmetric cavities of 40 µm cavity length. a) is with SM fiber mirrors and b) is with SM GRIN assemblies. We can see the improved coupling depth when a SM GRIN assembly is used.

Conclusion and Outlook

In my masters thesis I presented fabrication techniques and the realization of FFPCs with improved mode matching. This included building a microscope beam profiling system, which allowed us to reduce the characterization time of single assembly from previously 8 hours to only 10 minutes. This facilitated the characterization of large sets of SM-GRIN assemblies in order to optimize their fabrication e.g. the used fiber types or splicing and cleaving parameters. The new gained full 3 dimensional intensity profiles of the beams emitted from the fiber assemblies allow to include information on the emitted beam shape in terms of e.g. aberrations and beam ellipticity in the quality assessment of produced assemblies.

During the course of the thesis I closely worked with Santhosh Surendra on the CO_2 laser ablating setup, where I was involved in finding the optimal operation parameters to ablate different fiber types including assemblies. These required separate optimization since the heatflow in short GRIN pieces of various length can differ from that in normal fibers. Almost 200 bare SM fibers and 150 SM GRIN fiber assemblies were prepared and shot. These fibers were characterized and were sent for high reflection coating. The techniques to store, pack and ship these fibers and assemblies were also improved during my thesis.

We analyzed an ABCD matrix based model to characterize the emitted Gaussian beam profiles from SM-GRIN assemblies. It turned out that the effects of the fabrication itself need to be included for example by adding a splice damaged region between the fibers to be able to predict the emitted beam parameters. We also systematically characterized fabrication imperfections using this model. It can be concluded that the performance of the assemblies is very sensitive to cleave angles at the end facets that therefore have to be minimized. Also decentered ablation patterns strongly affect the later-on mode matching, which is why the shooting setup has to be improved to be more stable to avoid drifts in beam pointing. Since not all observed beam shapes were explainable using a model only including fundamental Gaussian beams, we started to also include higher order Laguerre modes in the analysis. However, this analysis are not conclusive and can be explored in the future. Finally, I built a FFPC that exhibited significantly better mode matching than possible without the use of fiber assemblies. The built cavity was made using an asymmetric geometry with a concave fiber mirror and a flat mirror substrate. The best performance ws achieved at a cavity length of 40 um which would correspond to an 80 um symmetric cavity geometry. For making longer symmetric cavities, we were limited by the alignment precision of the mirrors in free space and were not yet able to characterize the cavity with more than 70 μm of cavity length. One possible solution to this challenge is to build the

cavity using a ferrule-based technique developed by Carlos Saavedra . Using this technique however requires glass ferrules with a bore diameter that is exactly matching that of the inserted fiber mirror. The assemblies are somewhat harder to integrate because of their small diameter variation at the splice point. In the future these techniques will be further developed to improve alignment of these fibers so that longer symmetric cavities with mode matching can be fabricated.

Bibliography

[1]   A. Einstein, *Zur Quantentheorie der Strahlung, Physicalische Zeitschrift 18: 121–128. Translated in ter Haar, D.(1967)*, The Old Quantum Theory (1917) 167 (cit. on p. 1).

[2]   E. M. Purcell, H. C. Torrey, and R. V. Pound,
Resonance absorption by nuclear magnetic moments in a solid, Physical review **69** (1946) 37
(cit. on p. 1).

[3]   M. Steiner et al., *Single ion coupled to an optical fiber cavity*,
Physical review letters **110** (2013) 043003 (cit. on p. 1).

[4]   M. Fox, *Quantum optics: an introduction*, vol. 15, OUP Oxford, 2006 (cit. on p. 1).

[5]   M. Uphoff et al., *An integrated quantum repeater at telecom wavelength with single atoms in optical fiber cavities*, Applied Physics B **122** (2016) 46 (cit. on p. 1).

[6]   Y. Colombe et al.,
Strong atom–field coupling for Bose–Einstein condensates in an optical cavity on a chip,
Nature **450** (2007) 272 (cit. on p. 1).

[7]   R. Albrecht et al., *Narrow-band single photon emission at room temperature based on a single nitrogen-vacancy center coupled to an all-fiber-cavity*,
Applied Physics Letters **105** (2014) 073113 (cit. on p. 1).

[8]   N. Flowers-Jacobs et al., *Fiber-cavity-based optomechanical device*,
Applied Physics Letters **101** (2012) 221109 (cit. on p. 1).

[9]   G. K. Gulati et al., *Fiber cavities with integrated mode matching optics*,
Scientific Reports **7** (2017) 1 (cit. on p. 1).

[10] G. Gagliardi and H.-P. Loock, *Cavity-enhanced spectroscopy and sensing*, Springer, 2014
(cit. on p. 2).

[11] D. Röser, *Fiber Fabry-Perot Cavities for Quantum Information and Spectroscopy*, (2019)
(cit. on pp. 2, 9, 10, 16, 25).

[12] M. Kubista, *A New Fiber Mirror Production Setup*, (2017) (cit. on pp. 2, 6, 16).

[13] P. Milonni, J. Eberly, and E. coaut, *Lasers*, A Wiley-Interscience publication, Wiley, 1988,
ISBN: 9780471627319, URL: https://books.google.de/books?id=nxlRAAAAMAAJ
(cit. on pp. 3, 4).

[14] N. Ismail et al., *Fabry-Pérot resonator: spectral line shapes, generic and related Airy distributions, linewidths, finesses, and performance at low or frequency-dependent reflectivity*,
Optics express **24** (2016) 16366 (cit. on p. 3).

[15]   J. C. Gallego Fernández,
        Strong Coupling between Small Atomic Ensembles and an Open Fiber Cavity, (2018)
        (cit. on pp. 3, 4, 37).

[16]   FDominec, *A diagram of stability of an optical resonator. The parameters g1 and g2 are
        obtained as g1=1-(L/R1) and g2=1-(L/R2), where R is the mirror curvature radius and L is the
        resonator length.* File: `LambdaPlaques.jpg`, 2007,
        URL: https://en.wikipedia.org/wiki/Optical_cavity#/media/File:
        Laser_resonator_stability.svg (cit. on p. 5).

[17]   A. E. Siegman, *Lasers university science books*, Mill Valley, CA **37** (1986) 169 (cit. on p. 4).

[18]   D. Lorenser, X. Yang, and D. D. Sampson, *Accurate modeling and design of graded-index fiber
        probes for optical coherence tomography using the beam propagation method*,
        IEEE Photonics Journal **5** (2013) 3900015 (cit. on pp. 6, 20).

[19]   D. Hunger et al., *A fiber Fabry–Perot cavity with high finesse*,
        New Journal of Physics **12** (2010) 065038 (cit. on pp. 7, 8, 35).

[20]   Y. R. Sortais et al., *Diffraction-limited optics for single-atom manipulation*,
        Physical Review A **75** (2007) 013406 (cit. on p. 13).

[21]   W. Jung et al.,
        Numerical analysis of gradient index lens-based optical coherence tomography imaging probes,
        Journal of biomedical optics **15** (2010) 066027 (cit. on p. 19).

[22]   W. Joyce and B. DeLoach, *Alignment of Gaussian beams*, Applied optics **23** (1984) 4187
        (cit. on p. 22).

[23]   B. Brandstätter et al., *Integrated fiber-mirror ion trap for strong ion-cavity coupling*,
        Review of Scientific Instruments **84** (2013) 123104 (cit. on p. 35).

[24]   C. Saavedra et al., *Tunable Fiber Fabry-Perot Cavities with High Passive Stability*,
        arXiv preprint arXiv:2010.02204 (2020) (cit. on pp. 35–37).

[25]   S. Garcia et al., *Dual-wavelength fiber Fabry-Perot cavities with engineered birefringence*,
        Optics express **26** (2018) 22249 (cit. on p. 36).